Università degli Studi di Padova

DIPARTIMENTO DI FISICA E ASTRONOMIA "GALILEO GALILEI"

Corso di Laurea Magistrale in Fisica

Dynamical Formation of Intermediate-Mass Black Hole Binaries

Candidato:
Marco Dall'Amico

Relatori:
Prof. Michela Mapelli
Dott. Ugo N. Di Carlo

Padova, 6 Aprile 2020

Abstract

Observational evidence for intermediate-mass black holes (IMBHs) has long been sought. With a mass $\sim 10^{2-5}$ $M_\odot$, IMBHs are expected to bridge the gap between stellar-born black holes (BHs) and super-massive black holes lying at the center of galaxies. In this work, we present a dynamical study of IMBHs in which we aim to address the formation scenarios of these objects and of IMBH binaries (IMBHBs, i.e. binaries that include at least one IMBH) in young massive star clusters. Specifically, we simulated 10^4 three-body interactions between a binary black hole (BBH) and a massive $\geq 60\,M_\odot$ BH with ARWV, a direct N-body code that exploits the Mikkola's algorithm for regularization, post-Newtonian parameters up to the 2.5 order and a relativistic kick prescription for mergers. After 10^5 yr of interactions, we obtain that the $\sim 3.8\%$ of the simulated systems merge within a Hubble time, while the $\sim 0.6\%$ reach the coalescence during the interaction. Dynamical encounters increase the number of massive mergers up to $\sim 1.5\%$ for BBHs with at least one pair-instability BH component, and up to $\sim 0.5\%$ for IMBHBs after a three-body encounter. Moreover, dynamical interactions produce in 0.01% of the cases a second-generation BBH born from a merger remnant BH and a binary of IMBHs, which both merge within a Hubble time. All the resulting binaries have, on average, higher total and chirp masses and lower mass ratios than the initial conditions, and have eccentricities close to one. In view of these results, we can conclude that dynamics plays a major role in IMBH production and evolution in young massive star clusters.

Contents

Introduction

The first gravitational wave detection GW150914 marked the beginning of a new era for multi-messenger astronomy. So far, ten binary black holes (BBHs) and two double neutron stars (DNSs) have been observed by the LIGO and Virgo interferometers (The LIGO–Virgo Collaboration 2019 [84] & 2020 [87]). Although our data sample is still limited, these twelve detections have already led to break-through results in several branches of physics. One of the most important implications of this discovery is not just the direct proof of the existence of stellar-mass black holes (BHs), but also the confirmation that these objects can be part of binary systems and merge within a Hubble time producing more massive BHs.

On the one hand, the existence of stellar-mass BHs has been proved by these recent gravitational wave observations; on the other hand, the first picture of the supermassive black hole (SMBH) M87 produced by the Event Horizon Telescope (2019 [83]) has confirmed the existence of these monsters lying at the centre of galaxies. These data on both stellar-mass BHs and SMBHs have helped us to better constrain the upper and lower ends of the poorly-known black hole mass spectrum, but we still miss information for the intermediate-mass range $10^2 \leq m_{BH}/M_{\odot} \leq 10^5$ where black holes can be considered intermediate-mass black holes (IMBHs).

IMBHs are the focus of this work, and we aim to study their dynamical formation, evolution and growth in mass via three-body interactions. Specifically, we performed 10^4 simulations of dynamical encounters between a BBH and a massive BH to study all the possible outcomes that can follow as result from a three-body encounter. With respect to most of the previous works (e.g. Hamilton & Miller [61], Giersz et al. 2015 [23], Rasskazov et al. 2019 [71]), our simulations are set in young massive star clusters and have been run with the direct N-body code ARWV. ARWV exploits the Mikkola's algorithm for regularization and implements a post-Newtonian treatment of the acceleration equations up to the third order for a better description of the close encounters between BHs.

We simulated our systems for 10^5 years and we found 436 binaries with $t_{coal} \leq 13.8\,Gyr$, $\sim 12.6\%$ of which merge during the simulation, while $\sim 42.0\%$ are formed as a consequence of exchange interaction, $\sim 45.0\%$ are perturbed by the intruder in a fly-by encounter and $\sim 0.23\%$ are born as

second-generation BBHs from a merger event. These binaries have more massive BH components and chirp masses with respect to the initial binary systems. Furthermore, dynamics drastically changes the binary properties in favor of low values of mass ratios and eccentricities close to one. Finally, 153 of the simulated merging binaries have one of the two BHs in the pair-instability mass gap, 54 are IMBH binaries one of which is a binary composed of two IMBHs.

Chapter 1

Massive Stellar Black Holes Observations

All binary black hole (BBH) mergers detected so far are characterized by masses in the stellar-mass range, while only little is known for black holes with intermediate mass. In this chapter, we first resume the main properties of the 10 observed black hole (BH) mergers by LIGO and Virgo, and we then discuss the observational implications of intermediate-mass black holes (IMBHs).

1.1 Gravitational Wave BBHs Detections

The discovery of gravitational waves provided us a powerful tool for surveying the population of BHs across the Universe. Observing gravitational waves is currently possible thanks to the advanced LIGO and Virgo gravitational-wave observatories, which form the first three-detector network of ground-based interferometers. These detectors are sensitive to gravitational-wave signals generated by the inspiral, merger and ringdown phases of compact binary coalescences, covering a frequency range from 15 Hz up to few kHz. The two LIGO facilities of Hanford and Livingstone, and (since August 2017) the Virgo interferometers in Italy detected a total of ten gravitational wave signals emitted from the coalescence of BBHs, three of which in the first observative run (O1) carried out from September 12, 2015, to January 19, 2016, and seven in the second run (O2) performed from November 30, 2016, to August 25, 2017[1]. The main properties inferred from the observations of these 10 detections are reported in table 1.1. The observed BBHs ranges from a total mass of $18.6^{+3.2}_{-0.7}\,M_{\odot}$ (for GW170608) up to $84.4^{+15.8}_{-11.1}\,M_{\odot}$ (for GW170729), and their BH remnant masses from $17.8^{+3.4}_{-0.7}\,M_{\odot}$ up to $79.5^{+14.7}_{-10.2}\,M_{\odot}$ in the source frame. Four of the merger products (GW150914,

[1]The third observing run (O3) of advanced LIGO and Virgo began on April 1, 2019.

Event	m_1 $[M_\odot]$	m_2 $[M_\odot]$	$\mathcal{M}$ $[M_\odot]$	χ_{eff}	E_{rad} $[M_\odot c^2]$	ℓ_{peak} $[10^{56}\,erg\,s^{-1}]$	d_L Mpc	z	$\Delta\Omega$ $[deg^2]$
GW150914	$35.6^{+4.7}_{-3.1}$	$30.6^{+3.0}_{-4.4}$	$28.6^{+1.7}_{-1.5}$	$-0.01^{+0.12}_{-0.13}$	$3.1^{+0.4}_{-0.4}$	$3.6^{+0.4}_{-0.4}$	440^{+150}_{-170}	$0.09^{+0.03}_{-0.03}$	182
GW151012	$23.2^{+14.9}_{-5.5}$	$13.6^{+4.1}_{-4.8}$	$15.2^{+2.1}_{-1.2}$	$0.05^{+0.31}_{-0.20}$	$1.6^{+0.6}_{-0.5}$	$3.2^{+0.8}_{-1.7}$	1080^{+550}_{-490}	$0.21^{+0.09}_{-0.09}$	1523
GW151226	$13.7^{+8.8}_{-3.2}$	$7.7^{+2.2}_{-2.5}$	$8.9^{+0.3}_{-0.3}$	$0.18^{+0.20}_{-0.12}$	$1.0^{+0.1}_{-0.2}$	$3.4^{+0.7}_{-1.7}$	450^{+180}_{-190}	$0.09^{+0.04}_{-0.04}$	1033
GW170104	$30.8^{+7.3}_{-5.6}$	$20.0^{+4.9}_{-4.6}$	$21.4^{+2.2}_{-1.8}$	$-0.04^{+0.17}_{-0.21}$	$2.2^{+0.5}_{-0.5}$	$3.3^{+0.6}_{-1.0}$	990^{+440}_{-430}	$0.20^{+0.08}_{-0.08}$	921
GW170608	$11.0^{+5.5}_{-1.7}$	$7.6^{+1.4}_{-2.2}$	$7.9^{+0.2}_{-0.2}$	$0.03^{+0.19}_{-0.07}$	$0.9^{+0.0}_{-0.1}$	$3.5^{+0.4}_{-1.3}$	320^{+120}_{-110}	$0.07^{+0.02}_{-0.02}$	392
GW170729	$50.2^{+16.2}_{-10.2}$	$34.0^{+9.1}_{-10.1}$	$35.4^{+6.5}_{-4.8}$	$0.37^{+0.21}_{-0.25}$	$4.8^{+1.7}_{-1.7}$	$4.2^{+0.9}_{-1.5}$	2840^{+1400}_{-1360}	$0.49^{+0.19}_{-0.21}$	1041
GW170809	$35.0^{+8.3}_{-5.9}$	$23.8^{+5.1}_{-5.2}$	$24.9^{+2.1}_{-1.7}$	$0.08^{+0.17}_{-0.17}$	$2.7^{+0.6}_{-0.6}$	$3.5^{+0.6}_{-0.9}$	1030^{+320}_{-390}	$0.20^{+0.05}_{-0.07}$	308
GW170814	$30.6^{+5.6}_{-3.0}$	$25.2^{+2.8}_{-4.0}$	$24.1^{+1.4}_{-1.1}$	$0.07^{+0.12}_{-0.12}$	$2.7^{+0.4}_{-0.3}$	$3.7^{+0.4}_{-0.5}$	600^{+150}_{-220}	$0.12^{+0.03}_{-0.04}$	87
GW170818	$35.4^{+7.5}_{-4.7}$	$26.7^{+4.3}_{-5.2}$	$26.5^{+2.1}_{-1.7}$	$-0.09^{+0.18}_{-0.21}$	$2.7^{+0.5}_{-0.5}$	$3.4^{+0.5}_{-0.7}$	1060^{+420}_{-380}	$0.21^{+0.07}_{-0.07}$	39
GW170823	$39.5^{+11.2}_{-6.7}$	$29.0^{+6.7}_{-7.8}$	$29.2^{+4.6}_{-3.6}$	$0.09^{+0.22}_{-0.26}$	$3.3^{+1.0}_{-0.9}$	$3.6^{+0.7}_{-1.1}$	1940^{+970}_{-900}	$0.35^{+0.15}_{-0.15}$	1666

Table 1.1: Properties of the observed BH mergers by LIGO/Virgo reported in the GWTC-1 catalog (The LIGO/Virgo Scientific Collaboration 2019 [84]). Columns in order from left: Event name, primary BH mass, secondary BH mass, Chirp mass, dimensionless effective aligned spin, radiated energy, peak luminosity, luminosity distance, redshift and sky localization, which is the sky area of the 90% credible region.

GW170729, GW170818 and GW170823) are BHs with mass $\geq 60\,M_\odot$ above the lower end of the pair-instability mass gap. The distances range between 320^{+120}_{-110} Mpc (for GW170608) and 2840^{+1400}_{-1360} Mpc (for GW170729), while all the systems present only weakly constrained spins (we will return to these spin measurements in the next chapters). From these properties, Abbott et al. (2019 [84]) were able to infer a merger rate of $9.7 - 101\,\mathrm{Gpc^3\,yr^{-1}}$ within 90% credible interval for BBHs with stellar-mass BH components.

1.2 IMBH observations

Intermediate-mass black holes (IMBHs) are a class of BHs characterized by a mass in the range $10^2 \leq m_{BH}/M_\odot \leq 10^5$, too large to be considered stellar-mass BHs and too small to be classified as supermassive black holes (SMBHs). Proving their existence is pivotal to understand the link between these two distinct families of BHs and to explain the seeds of SMBH formation. IMBHs are also considered as the cause of several accretion and tidal disruption events, and their discovery would help to elucidate not only these phenomena but also their role in the dynamical evolution of dense stellar systems such as clusters of galaxies. Nevertheless, besides being supported by strong theoretical implications (that we will explore in the next chapters),

the existence of IMBHs is still controversial and is supported only by poor electromagnetical observational constraints. In appendix A we report a list of the best up to date IMBH candidates in the range $10^2 \leq m_{BH}/M_\odot \lesssim 10^5$ presented by Greene et al. (2019 [24]). The main electromagnetic observational techniques that are currently exploited to detect IMBHs are the following (Mezcua 2017 [55], Koliopanos 2018 [39]):

- Dynamical measurements of stars or direct monitoring of gas motion orbiting near a central BH are the most used techniques to detect the presence of an IMBH and reduce its mass. However, this method requires a spatial resolution high enough to completely solve the stellar and gas motion in the region close to the BH, which can currently be achieved only for systems as far as few Mpc.

- For systems that present a broad lines spectrum, it is possible to exploit the reverberation mapping method to reduce the velocity v of the gas in the broad-line region and consequently the central BH mass with the virial product $m_{BH} \simeq c\tau v^2/G$. The mass can be derived by measuring the delay τ between the continuum emitted by the BH accretion disk and the spectral lines emitted by the broad-line region. The main issue of this technique is that it works only for BHs surrounded by a large accretion disk energetic enough to drive broad line emission in the nearby region. Furthermore, reverberation mapping requires multi-epoch observations in order to measure the spectral time lag.

- BH accretion invariably generates X-ray emission. Observationally, the X-ray luminosity and the radio continuum luminosity closely scale with m_{BH}, such that these three quantities can be combined in the so-called fundamental plane. The BH mass can be thus reduced with this technique if the source emits a flux in both of these wavelengths.

- The mass of a massive BH harbored in the bulge of a galaxy is related to the velocity dispersion of the bulge stellar population with the $m_{BH} - \sigma_{bulge}$ scaling, or directly to the bulge luminosity with the Magorrian relation $m_{BH} - L_{bulge}$. These relations can be applied just to the lower end of the IMBHs mass range, i.e. on BHs with $m_{BH} \gtrsim 10^5\, M_\odot$.

For what concerns gravitational wave observations, the LIGO and Virgo Scientific Collaborations (Abbott et al. 2019 [2]) have recently reviewed the observational data of the first and second observative runs in search of binaries with at least one IMBH among the components. They found no such systems and they thus placed an upper limit of 0.20 $\mathrm{Gpc}^{-3}\ \mathrm{yr}^{-1}$ in comoving units at the 90% confidence level for binaries with mass components $m_1 = m_2 = 100\, M_\odot$ and dimensionless spins $\chi_1 = \chi_2 = 0.8$ aligned with the orbital angular momentum of the binary.

This lack of IMBH observations comes also from the fact that mergers of medium ($10^3 \leq m_{BH}/M_\odot \leq 10^4$) and upper-range ($10^4 \leq m_{BH}/M_\odot \leq 10^5$) IMBHs are outside the sensitivity band of the current generation of detectors. The next generation of gravitational wave observatories will be able not only to extend the observational mass window, but also to compute multiband gravitational wave astronomy as shown in figure 1.1. With space-based observatories such as the Laser Interferometer Space Antenna (LISA), we will be able to observe merging couples of BHs from the spiraling phase in the mHz regime down to the merger phase in the hHz, where the new ground-based interferometers such as LIGO A+ and Voyager, the Einstein Telescope and the Cosmic Explorer will operate with improved sensitivity.

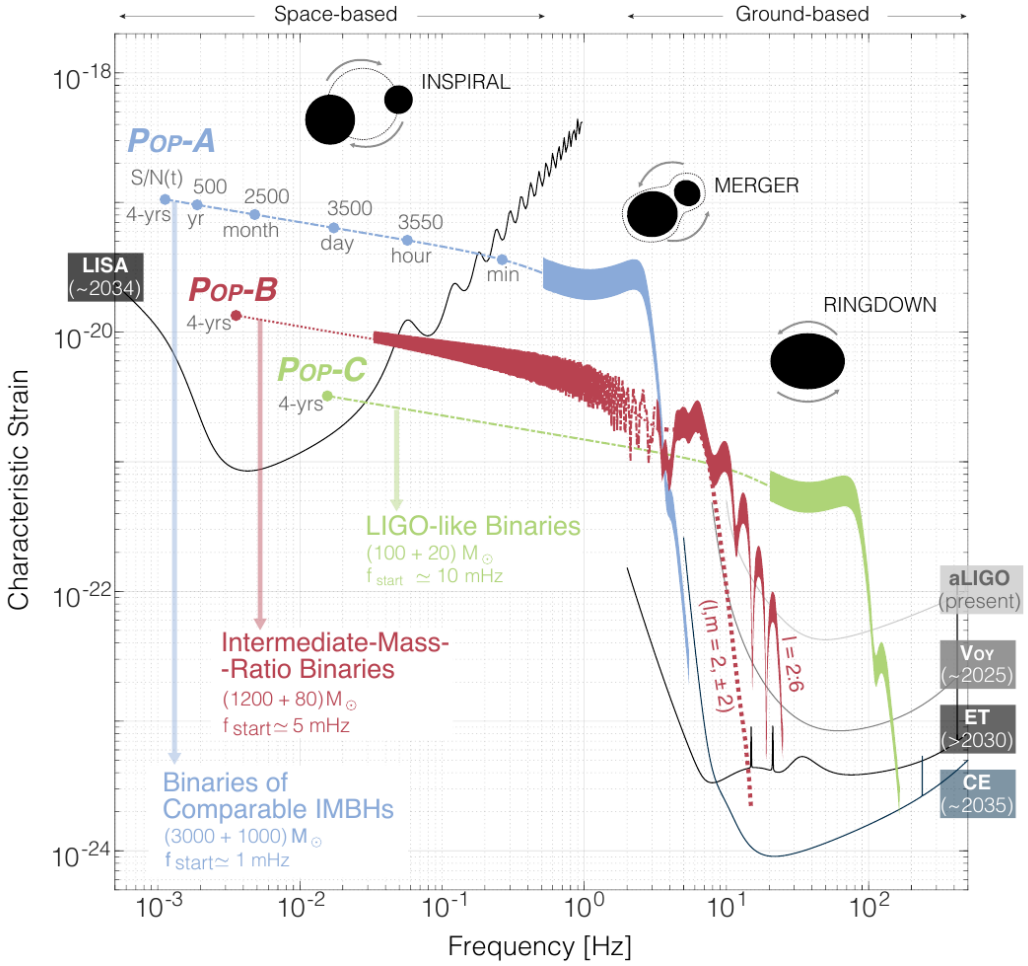

Figure 1.1: Multiband gravitational wave spectrum from Jani et al. (2019 [34]). The plot shows the sensitivity bandwidths of the next generation of gravitational wave detectors, and the characteristic signals of three different populations of binaries containing at least one IMBH. Pop-A is composed of BBHs with two mid-range IMBHs as components, Pop-B is composed of BBHs with an IMBH and a stellar-mass BH, while Pop-C includes BBHs with both components in the stellar-born mass range.

Chapter 2

Dynamical Formation Channel: the Three-Body Interaction

In the last chapter, we have seen that stellar-mass black hole binaries (BBHs) can merge within a Hubble time and give birth to massive black holes. We want now to present where and how these binary systems form and evolve. In particular, in this chapter we present the dynamical formation channel for BBHs which can consequently evolve to intermediate-mass black hole binaries (IMBHBs). We start from the description of active dynamical environments such as star clusters and move on to the explanation of the three-body encounters with the relative outcomes.

2.1 Star Clusters

2.1.1 Properties and Evolution

In this work, we aim to study the effect of dynamics on three-body encounters of black holes. Thus, we need to set up our simulations in an environment whose properties allow three-body encounters to occur, such as star clusters. Star clusters (SCs) are defined as collisional particle systems, which means that dynamical interactions among particles are efficient and the two-body relaxation can occur within the cluster lifetime. SCs are divided mainly in function of their properties such as age, mass, and size. The age of a SC is strictly related to the age of its stars and can be observationally derived computing the turn-off point in the Hertzsprung-Russel diagram. Assuming that the virial theorem holds, the mass of a SC is determined with the following expression

$$M_{vir} = \eta \left(\frac{\sigma_{1D}^2 \, r_{eff}}{G} \right) \tag{2.1}$$

where η is a constant related to the density profile of the SC, while σ_{1D} and

r_{eff} are two observable quantities defined respectively as the one dimensional line-of-sight velocity dispersion and the effective radius, which is the projected radius containing half of the cluster luminosity. Massive SCs are nearly spherical systems, therefore it is possible to define a variable that describes theoretically or observationally their radius. One possibility is given if a system with mass M satisfies the virial theorem, in which case it is possible to define the virial radius as

$$r_{vir} = \frac{GM^2}{2|U|} \tag{2.2}$$

where U is the total potential energy. Finally, the spatial size of the SC can be expressed also with the half-mass radius r_{hm}, defined as the spatial distance from the center containing half of the cluster total mass.

SCs are complex systems whose evolution strictly depends on the evolution of their stellar population. We can thus identify three main phases in the lifetime of a SC:

I. The first phase of a SC is characterized by violent star formation episodes while the gas is still abundant in the cluster. This stage ends $\sim 3\,Myr$ after the formation, when the first supernova events start to take place and sweep the gas from the cluster with the help of stellar winds and radiation of OB stars.

II. In the second stage, the cluster is largely gas-free, while stellar mass loss plays an important role in the overall dynamics. The end of this stage strictly depends on the initial mass, radius, density profile and initial mass function of the cluster and it could range from $100\,Myr$ to $1\,Gyr$.

III. In the last phase the gas is totally expelled from the cluster, and the evolution is purely dominated by dynamical interactions.

The main driver of SCs dynamical evolution is the two-body relaxation. In a particle system dominated by gravity, the mutual long range interactions between particles cause the redistribution of the energy and, as a result, the system moves toward the energy equipartition. This process is characterized by the two-body relaxation timescale t_{rlx}, defined as the time in which the stars of a cluster lose memory of their initial velocities because of their mutual gravitational interactions. The expression for this timescale is (Spitzer 1971 [80])

$$t_{rlx} = \frac{N}{8 \ln N} \frac{r}{v} \tag{2.3}$$

where N is the number particle of the system, while r and v are the radius and the typical velocity of the cluster. This timescale will be resumed in the next chapter (section 3.2), because it has great importance in the formation of IMBHs by runaway collisions.

Another important timescale is the dynamical timescale, defined as the time in which a particle crosses the system from part to part. This can be expressed as (Portegies Zwart & McMillan 2010 [68])

$$t_{dyn} = \frac{GM^{5/2}}{(-4E)^{3/2}} \sim 2 \times 10^5 \, yr \left(\frac{M_{cl}}{10^4 M_\odot} \right)^{-1/2} \left(\frac{r_{vir}}{1 \, pc} \right)^{3/2}. \tag{2.4}$$

In the left expression, $E = T + U$ is the total energy. The right expression has been derived assuming the virial theorem, i.e. that $2T + U = 0$ with T and U kinetic and potential energy of the cluster. The dynamical timescale determines also the time that the system takes to reach the dynamical equilibrium.

Another fundamental dynamical process that takes place in a SC is the core-collapse phenomenon. For a star cluster with a realistic mass function, this is directly related to the two-body relaxation timescale, and it can be written as (Portegies Zwart & McMillan 2002 [66])

$$t_{cc} \sim 0.2 \, t_{rlx} \tag{2.5}$$

Thus core-collapse happens even before the two-body relaxation. The two-body relaxation acts as a machinery to transfer kinetic energy from the inner to the outer regions of the cluster. Furthermore, in the inner regions, high-velocity stars are expelled (evaporation process) from the cluster. Their ejection reduces the potential energy and even more the kinetic energy of the central regions since they are the fastest particles in the velocity distribution tail. A star cluster is in equilibrium as long as $2T + U = 0$. The two-body relaxation and the evaporation process lead, therefore, the inner regions to break the equilibrium since they cause a net decrease of kinetic energy, leading to $2T + U < 0$. As result, the core starts to contract in a runaway scenario known as gravothermal instability. Since SCs are systems with negative heat capacity, the contraction leads the core to heat up while the outer regions of the cluster expand. The result of this process is that the dispersion velocity of the stars in the core is drastically increased. This causes more escapers to subtract even more kinetic energy from the core, which accelerates toward infinite density. However infinite density is not a physical quantity and, moreover, we observe SCs in post core-collapse stages. There must exist a source of energy able to contrast the core collapse and to restore the virial equilibrium. This energy is the one provided by three-body interactions between stars. What happens in fact, is that as the density increases while the core collapses, the probability of encounters between stars

becomes higher and higher. As we will see in section 2.2.1, hard binaries are tight binaries that, as a consequence of interactions with other bodies, tend to reduce their internal energy even more increasing the kinetic energy of the three-body center-of-mass. They, therefore, represent a source of heating for the system, which can finally stop the core collapse and restore the equilibrium.

The core-collapse is a phenomenon that occurs even if the system is composed of particles with equal mass. In the real world, SC particles are characterized by a spread mass spectrum. This variety in mass has the effect to accelerate even more the dynamical evolution and the core-collapse phase of the cluster. In fact, the more massive objects of a cluster experience a drag force exerted by lighter objects in their surroundings. This drag force makes massive objects to decelerate, and as a consequence they then start sinking toward the cluster core attracted by the center of the potential well. This process is known as mass segregation, and occurs in a timescale

$$t_{mass\ segregation} = \frac{\langle m \rangle}{M} t_{rlx} \tag{2.6}$$

where $\langle m \rangle$ is the average mass of the cluster and M is the mass of the massive object. We will return to the mass segregation effect in the next chapter with the explanation of runaway collisions.

2.1.2 Star Clusters Types

SCs can mainly be divided into four categories: *globular clusters*, *open clusters*, *nuclear clusters* and *young massive clusters*. Globular clusters (GCs) are old metal-poor clusters that host Population II stars, and were born $\sim 12\,Gyr$ years ago. They are characterized by large masses that span from $\sim 10^3\,M_\odot$ (for AM4, member of the Sgr dwarf spheroidal galaxy) up to $2.2 \times 10^6\,M_\odot$ (for NGC5139 Omega Centauri). Nearly 150 GCs are known in the Milky Way and they are found orbiting in galaxy halos. Another family of clusters is the open clusters (OCs), which can count more than 1100 elements only in the Milky Way. These are young clusters with an age that can vary from few hundreds of Myr up to few Gyr, and are composed of few thousands of Population I stars loosely bound together. Open clusters are important because they are the end products of recent star formation episodes, thus their stars have nearly the same age, chemical composition, and Earth distance. Furthermore, OCs are the main nurseries for massive stars. Another type of SCs are the nuclear star clusters (NCs). These are luminous and massive clusters with $m_{cl} \sim 10^6 - 10^8\,M\odot$ and effective radii $2 - 5\,pc$, and they are characterized by extremely high densities $\sim 10^6\,M_\odot\,pc^{-3}$ such that their escape velocities reach values up to $40\,km\,s^{-1}$. NCs experience

cluster	age [Gyr]	M [$M_\odot$]	r_{vir} [pc]	ρ_c [$M_\odot/pc$]	Z [$Z_\odot$]	location	t_{dyn} [Myr]	t_{rlx} [Myr]
OC	$\lesssim 0.3$	$\lesssim 10^3$	1	$\lesssim 10^3$	~ 1	disk	~ 1	$\lesssim 100$
GC	$\gtrsim 10$	$\gtrsim 10^5$	10	$\gtrsim 10^3$	< 1	halo	$\gtrsim 1$	$\gtrsim 1000$
NC	$\gtrsim 10$	$\gtrsim 10^6$	5-10	$\gtrsim 10^5$	≤ 1	bulge	$\gtrsim 1$	$\lesssim 10000$
YMC	$\lesssim 0.1$	$\gtrsim 10^4$	1	$\gtrsim 10^3$	$\lesssim 1$	galaxy	$\lesssim 1$	$\lesssim 100$

Table 2.1: Indicative properties of open clusters (OC), globular clusters (GC), nuclear clusters (NC) and young dense massive star clusters (YMC). The first column is the cluster type, the second is the age of the cluster, followed by the total cluster mass, the virial radius, the core density, the metallicity, the typical location where they can be found in a galaxy, and the dynamical and relaxation timescales as last two. The table comes from Portegies Zwart & McMillan, 2010, [68].

multiple epochs of star formation and are found in almost all types of galaxies ($\sim 50-75\,\%$ of all galaxies), usually settled in the galaxy core orbiting in the neighborhood of a supermassive black hole. Besides these categories of star clusters, there is a fourth type that shares some characteristics of GCs and OCs: these are the *young dense massive star clusters* (YMCs). Following the definition of Portegies Zwart & McMillan (2010 [68]), we define these clusters as young since they are still in the mass-loss phase in the fist $100\,Myr$. They are considered dense because their half-mass relaxation time (i.e. t_{rlx} defined with r_{hm}) is less than $\sim 10^8\,yr$. YMCs mass is high enough to ensure the cluster to survive up to $\sim 10\,Gyr$, i.e. in the old globular cluster regime. Twelve clusters in the Milky Way satisfy these conditions and are considered YMCs, while many others are observed in the local group and beyond (e.g. for a catalog see Portegies Zwart & McMillan 2010 [68]). Their spatial distribution is compared to that of GCs and OCs in figure 2.1, while the main properties are summarised in table 2.1.

We decided to focus on YMCs because they are characterized by the following features:

- With respect to GCs, YMCs are still young and star formation is still at work (Lada & Lada 2003 [42]). Star formation is extremely important since it gives birth to massive stars that will die in few Myr, supplying the cluster with massive stellar BHs which will likely participate to the cluster dynamics via three-body encounters. Furthermore, YMCs are characterised by smaller relaxation times than GCs (see Table 2.1), and this implies that core-collapse (Eq. 2.5) and mass segregation (Eq. 2.6) happen earlier. Both these phenomena have the effect of increasing the

core density of the cluster and, since the interaction rate scales as the density, this implies that three-body encounters between black holes will occur more frequently after these processes. Therefore dynamical interactions are favored at earlier times in YMCs than in GCs.

- With respect to OCs, YMCs are more massive. More massive clusters have higher chances of surviving the early gas-ejection phase (avoiding the so-called infant mortality) Therefore YMC lifetime is predicted to be longer than the one of OCs, ensuring more time in which dynamical interactions between black holes can take place. Furthermore, YMCs are much denser than OCs, and this increases again the encounter probability between cluster objects.

- NCs are other possible birthplace candidates for IMBHs since their high masses allow frequent interactions between BHs, while on the other hand, the high escape velocities retain more escaping BHs. Despite these considerations, the huge computational resources required for NCs simulations make these objects only poorly studied.

2.2 BBH Formation via three-body encounters

There are two main theoretical scenarios that can lead to the formation of a binary of black holes. One is the binary evolution scenario, in which two stars in an isolated original[1] binary system evolve and give birth to a black hole each, creating a BBH if the system is able to survive through the different phases of the evolution. This formation channel has been largely studied with population-synthesis codes (Tauris et al. 2015 [82], Mapelli & Giacobbo 2018 [53], Spera et al. 2018 [79]), but still includes several theoretical issues mainly related to the common envelope phase, the kick imparted to the new-born black holes and the various mass transfer cases. The second BBH formation channel is the dynamical scenario, in which the dynamics of a star cluster can drive the formation and evolution of compact-object binaries via dynamical encounters. The main issue of this formation channel is that we have to deal with the N-body problem, which is extremely expensive to be treated computationally since it requires the usage of N-body codes. On the other hand, the main advantage of the dynamical scenario is that BBHs, after their birth, can still grow in mass and reduce their semi-major axis as effect of dynamical interactions. Therefore, in a dynamical active environment BBHs can become more and more massive due to exchanges until they evolve to IMBHBs. For these reasons, we will focus the next section on the formation of BBHs and IMBHs by three-body encounters. In

[1] By original binary we mean a binary which components are stars bound since their birth.

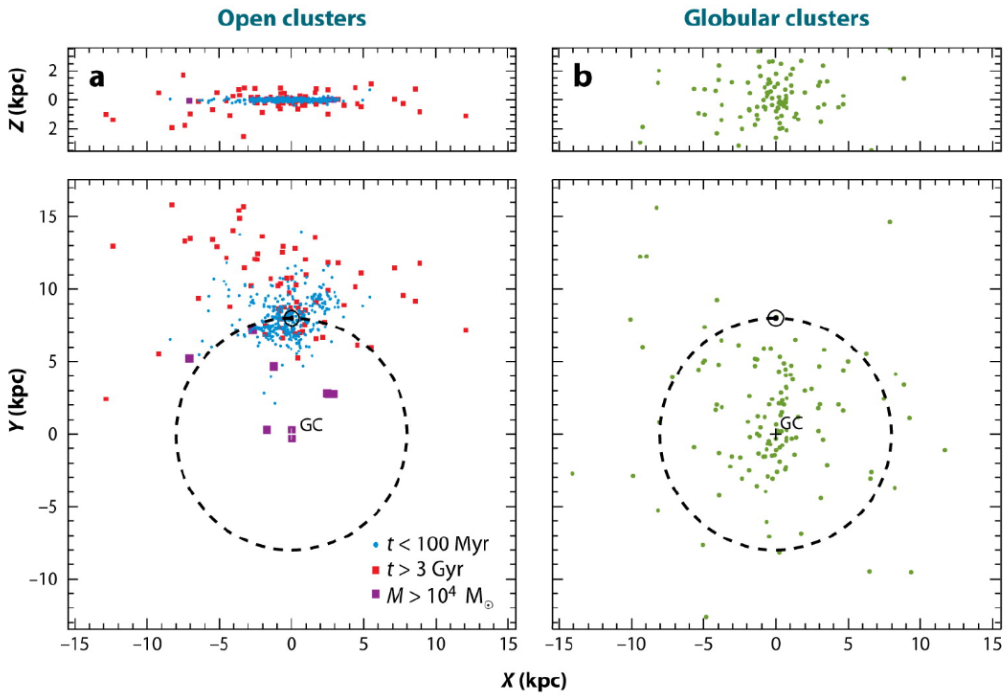

Figure 2.1: Spatial distribution of SCs in the Milky Way seen respectively edge-on (top) and face-on (below) from Portegies Zwart & McMillan, 2010, [68]. Left: the distribution for young (blue dots) OCs, old (red dots) OCs, and YMCs (purple boxes). Right: same but for GCs. The black dashed line represents the sun orbit around the galactic center while the small black circle shows the sun's position. In the left panel, OCs and YMCs seem distributed mainly in the solar neighborhood, but this is an observational selective effect caused by galactic extinction. Lastly, from the top pannels, it is clearly visible that GCs are distributed in the galactic halo while younger clusters are concentred in the galactic disk.

principle, energy dissipation caused by gravitational waves can form a binary from a two-body encounter of two black holes. Therefore an IMBH could hypothetically bind with another black hole to form an IMBHB, but this case is very unlikely. Lastly, interactions with more than three bodies can occur, but we decided to limit our simulations to the three-body interaction case since it is the most probable encounter scenario (Heggie 1975 [28]).

2.2.1 Three-Body encounters

We define three-body encounters as dynamical interactions between a single object and a binary system. The main difference with the two-body encounter scenario is given by the fact that in this case the interaction involves a binary, and energy exchanges between the internal energy of the binary and the kinetic energy of the single object[2] are allowed. The total energy of a binary system is defined as

$$E_{tot} = \frac{1}{2}\mu v^2 - \frac{Gm_1m_2}{r}. \tag{2.7}$$

The first term is the kinetic energy of the system center-of-mass E_k as a function of the reduced mass of the system $\mu = (m_1m_2)/(m_1 + m_2)$, where m_1 and m_2 are respectively the primary and secondary star. The second term represents instead the internal energy of the system E_i, which is the energy reservoir of the binary. This energy can be exchanged in a dynamical encounter and is defined as the inverse of the binary binding energy $E_b = -E_i$. If the system is bound the total energy is negative $E_{tot<0}$, and the binary system has an elliptical orbit with semi-major axis a and eccentricity e. The binding energy can be therefore rewritten as

$$E_b = \frac{Gm_1m_2}{2a}. \tag{2.8}$$

As a result of energy exchanges between a binary and a single star in a three-body interaction, several outcomes are possible: *hardening*, *dynamical ejection*, *exchange* and *ionization*. Finally, three-body interactions can also be resonant and set in *hierarchical-triple systems* in which the *Kozai-Lidov* oscillations can take place. Before moving on with the explanation of each of these processes, it is important to define the concepts of hard and soft binaries for a SC characterized by velocity dispersion σ and average star mass $\langle m \rangle$:

- *Hard binaries* are defined as binaries whose binding energy is higher with respect to the average star $\langle m \rangle$ kinetic energy, i.e.

$$\frac{Gm_1m_2}{2a} > \frac{1}{2}\langle m \rangle \sigma^2$$

[2] in next sections, we will refer to the third body also as the "intruder" object.

- *Soft binaries* are defined as binaries whose binding energy is lower with respect to the average star $\langle m \rangle$ kinetic energy, i.e.

$$\frac{Gm_1m_2}{2a} < \frac{1}{2}\langle m \rangle \sigma^2$$

The outcomes of a three-body interaction strictly depend on the energy exchanges of the process, and wether a binary will gain or lose binding energy can be predicted only in a statistical sense. Heggie (1975 [28]) developed the analytical formalism with the first numerical simulations to find the following important result known as Heggie's law

Heggie's law - Hard binaries statistically tend to harden, which means that in a dynamical encounter they will likely increase their binding energy (e.g. the intruder can extract internal energy from the binary which causes a decrease of the semi-major axis of the system, or an exchange event can introduce a more massive body in the binary increasing E_b). Soft binaries statistically tend to soften, or in other words they will likely decrease their binding energy as a result of a dynamical interaction (this happens if the binary gains internal energy at the expense of the kinetic energy of the intruder).

2.2.2 Hardening

We define a hardening process as a three-body interaction in which an intruder object extracts energy from the internal energy E_i of the binary. As a result of energy conservation, the extracted energy is used to increase the initial center-of-mass kinetic energy $E_{k,i}$ of the binary and the single object, leading to $E_{k,i} < E_{k,f}$. In this process, the internal energy of the binary becomes more negative while its initial binding energy $E_{b,i}$ grows. We have therefore that

$$E_{b,i} = \frac{Gm_1m_2}{2a_i} < \frac{Gm_1m_2}{2a_f} = E_{b,f} \tag{2.9}$$

which, in absence of mass transfer, implies that $a_f < a_i$, or namely that the orbital separation between the two components of the binary has shrunk due to the energy exchanges with the third object in the fly by process. Since after the encounter the kinetic energy of the center-of-mass has increased, both the binary and the intruder are subjected to a recoil. Sigurdsson & Phinney (1993 [76]) computed the recoil velocity of the binary system which can be expressed as

$$v_{rec} = \frac{m_3'}{(m_1+m_2+m_3)}\sqrt{\frac{m_3(m_1+m_2)}{m_3'(m_1'+m_2')}v_\infty^2 + \frac{2(m_1+m_2+m_3)}{m_3'(m_1'+m_2')}\Delta E_b} \tag{2.10}$$

where m_1', m_2' and m_3' are respectively the masses of the primary, secondary and intruder (they may change in the process, e.g. for an exchange), $v_\infty \sim \sigma$ and ΔE_b is the energy exchanged in the encounter. This recoil velocity may vary from few $km\,s^{-1}$ up to several hundreds of $km\,s^{-1}$, and it can cause the ejection of the binary if it exceeds the escape velocity of the cluster. When a binary is ejected into the field, it can no longer participate to the dynamic of the cluster, and it cannot evolve anymore to a BBH or IMBHB by other dynamical interactions. This effect is known as *dynamical ejection*, and as we will see in the next chapter it can also be caused by the relativistic kick produced in a merger event or by the recoil imparted to the remnant in a core-collapse supernova. Dynamical interactions are quite efficient in young star clusters because of their low escape velocities and can lead $\sim 40\%$ of the cluster black holes in being ejected (Mapelli et al. 2011 [49], Mapelli et al. 2013 [50]). Lastly, Monte Carlo simulations of GCs (Rodriguez et al. 2016 [72]) have shown that hardening processes are also important because binaries can acquire a significant eccentricity in the three-body process, which contributes to decrease their coalescence times and can lead them to merge within a Hubble time even if they are ejected from the cluster.
The following calculations of this sections are taken from Mapelli 2003 [47].

Now that we have defined the hardening process, we can explore in more detail its consequences and how these can affect the orbital evolution of the binary. First, we have to define the cross-section for a three-body encounter

$$\Sigma = \pi b_{max}^2. \tag{2.11}$$

This is defined as the area of a circle centered in the center-of-mass of the binary with radius b_{max} equal to the maximum impact parameter for which the energetic exchange with the intruder is not zero (Sigurdsson & Phinney 1993 [76]). In particular, the impact parameter is the minimum perpendicular distance between the orbit of the intruder and the center-of-mass of the binary. We can rewrite the cross-section under the assumptions that the binary is a hard binary which undergoes to a very energetic three-body encounter (i.e. the orbital pericenter of the intruder is very close to the semi-major axis of the binary $p \sim a$)

$$\Sigma = \frac{2\pi G(m1+m_2+m_3)a}{\sigma^2}. \tag{2.12}$$

It is important to notice that this cross section is much bigger with respect to the geometrical cross-sections of a binary system $\Sigma = \pi a^2$ or a single star

$\Sigma = \pi R_{star}^2$, therefore three-body interactions will dominate the encounters in a star cluster even if the binary fraction is low. We can now compute the hardening rate, i.e. the number of hardening processes per unit time that locally take place in a cluster with velocity dispersion σ and number density n:

$$\frac{dN}{dt} = n\Sigma\sigma = \frac{2\pi G(m1 + m_2 + m_3)\, n\, a}{\sigma}. \tag{2.13}$$

The rate of three-body encounters is, therefore, higher for massive objects, and this means that BHs dominate these interactions. Furthermore, it increases both with a because a binary has a larger cross-section, and with n because the interaction probability scales with the numerical density. Lastly, low dispersion velocities σ enhance the encounter rate. Combining the last equation with the average binding energy variation per encounter derived by numerical simulations (Hills 1983 [30]), we can rewrite equation 2.13 as a function of binding energy to find the rate of binding energy exchange for a hard binary. The average binding energy variation per encounter is

$$\langle \Delta E_b \rangle = \xi \frac{m_3}{m_1 + m_2} E_b. \tag{2.14}$$

The constant $\xi \sim 0.2 - 1$ is the post-encounter energy parameter which can be reduced from numerical simulations of three-body encounters (Quinlan 1996 [69]). The equation is another confirmation of Heggie's law since it states that three-body encounters between massive intruders and binaries with high binding energy will experience big energy exchanges, or in other words, hard binaries tend to harden. This expression has been derived by Hills making three assumptions: the binary must be hard, its pericenter needs to satisfy $p \lesssim 2a$ and the total mass of the binary must be greater than the mass of the single object, i.e. $m_1 + m_2 \gg m_3$. Finally, we can compute the rate of binding energy exchange for a hard binary

$$\frac{dE_b}{dt} = \langle \Delta E_b \rangle \frac{dN}{dt} = \frac{\pi \xi G^2 m_1 m_2 \rho}{\sigma} \tag{2.15}$$

with $\rho = n\langle m \rangle$ the average density of the cluster. The result is an equation that depends only on the masses of the binary components and on the cluster environments. If these properties do not change with time, the rate of binding energy exchanged for hard binaries is constant and this confirms that hard binaries harden at a constant rate. We can thus re-write equation 2.15 as a function of a plugging in the definition of binding energy (Eq. 2.8), this gives us a relation for the average time evolution of the semi-major axis of a hard binary

$$\left(\frac{da}{dt}\right)_{hard} = -2\pi G \xi \frac{\rho}{\sigma} a^2. \tag{2.16}$$

This is negative as expected since hardening must decrease the binary orbital separation. Since black holes are the most massive objects in the cluster, they belong to hard binaries which, due to Heggie's law, tends to harden even more as a consequence of three-body interactions. Hardening is therefore extremely important for BBHs since it is a dynamical process that reduces the orbital separation and consequently the time left for the merger. Nevertheless, equation 2.16 states that the lower is the semi-major axis, the lower is the cross-section of the binary and the less efficient the hardening processes become. Therefore, below a particular value of a, another process becomes efficient and this is the gravitational wave emission. Gravitational waves extract energy and momentum from the orbit of the two black holes, which as a consequence keep reducing their mutual distance, spiraling in to eventually merge. The description of the orbital evolution has been derived by Peters (1964 [64]), in particular, the semi-major axis and the eccentricity evolve with the time as

$$\left(\frac{da}{dt}\right)_{gw} = -\frac{64}{5}\frac{G^3 m_1 m_2 M_{tot}}{5a^3c^5}\frac{(1+73e^2/24+37e^4/96)}{(1-e^2)^{7/2}} \tag{2.17}$$

$$\left(\frac{de}{dt}\right)_{gw} = -\frac{304}{15}\frac{G^3 m_1 m_2 M_{tot}}{15a^4c^5}\frac{e(1+121e^2/304)}{(1-e^2)^{5/2}} \tag{2.18}$$

where $M_{tot} = m_1 + m_2$ and c is the speed of light. From the first expression, assuming that e does not change in time, it is possible to derive the coalescence time t_{coal}, defined as the time that a binary takes to reduce its initial semi-major axis a_0 to zero because of gravitational wave emission

$$t_{coal} = \frac{5}{256}\frac{a_0^4 c^5}{G^3 m_1 m_2 M}\frac{(1-e^2)^{7/2}}{(1+73e^2/24+37e^4/96)}. \tag{2.19}$$

When two black holes merge, they produce a more massive black hole that can dynamically interact with other black holes to form a second generation BBH. We can finally write a more general expression that takes into account for the two main drivers of the orbital evolution of an hard binary. Combining equation 2.16 and equation 2.17 we find (Mapelli 2018 [52])

$$\frac{da}{dt} \simeq -2\pi G\xi\frac{\rho}{\sigma}a^2 - \frac{64}{5}\frac{G^3 m_1 m_2 M_{tot}}{5(1-e^2)^{7/2}c^5}a^{-3} \tag{2.20}$$

In this equation, we can separate two different regimes in which hardening and GW emissions work to reduce a. Hardening processes dominate the evolution in the first phases of the binary evolution. When a is large, the first term in the equation is predominant and we have $da/dt \propto -a^2$. The second term takes over when a is small and hardening has already reduced enough

the semi-major axis. In this regime gravitational wave emission becomes efficient and $da/dt \propto -a^{-3}$. It is also important to notice that the hardening term, in contrast with GW emission, does not depend on eccentricity. A third regime actually exists between these two, when hardening processes become less efficient and GW emission is still ineffective. This is the regime in which a BBH spends most of its evolutive time. Figure 2.2 shows the evolution of a and the three regimes described by equation 2.17.

Finally, we can compute at which value of a, at which time and after which number of three-body interactions gravitational waves become the principal mechanism to tight the orbit. First, from equation 2.16, we can compute the hardening timescale as

$$t_{hard} = \left|\frac{a}{\dot{a}}\right| = \frac{\sigma}{(2\pi G\xi)}\frac{1}{a_{fin}}. \tag{2.21}$$

This is the time that a binary takes to reduce its semi-major axis to a_{fin} only via hardening processes. In the equation we neglected the initial value a_i resulting from the integration since for our purposes $a_i >> a_f$. Equating this timescale to t_{coal}, gives us the maximum semi-major axis value at which gravitational waves starts to dominate the evolution of a binary respect to hardening processes

$$a_{gw} = \left(\frac{256}{5}\frac{G^2 m_1 m_2 M \sigma}{2\pi\xi(1-e^2)^{7/2}c^5\rho}\right)^{1/5}. \tag{2.22}$$

Therefore, for binaries with $a \leq a_{gw}$ the main orbital-shrinking process is GW emission while for $a > a_{gw}$ the driver effect is hardening. Plugging a_{gw} in equation 2.21 as a_{fin}, it is possible to compute the time needed for a binary to enter in the GW regime as the effect of hardening semi-major axis reduction. Lastly, integrating equation 2.13, we can find the average total number of hardening encounters that a binary has experienced in a time t before entering in the GW regime

$$N_{hard} = \int_0^t \frac{dN}{dt}dt = \int_0^t \frac{2\pi G(m1 + m_2 + m_3)\, n\, a}{\sigma}\, dt. \tag{2.23}$$

we can now make a change of variable exploiting equation 2.16 and, integrating from a_i to a_{gw}, we find

$$N_{hard} = \frac{1}{\xi}\frac{(m_1 + m_2 + m_3)}{\langle m\rangle}\left(\frac{a_i}{a_{gw}}\right). \tag{2.24}$$

2.2.3 Exchanges

There is another mechanism that contributes to the production of binaries with higher binding energy. These are the *exchanges*, which are three-body

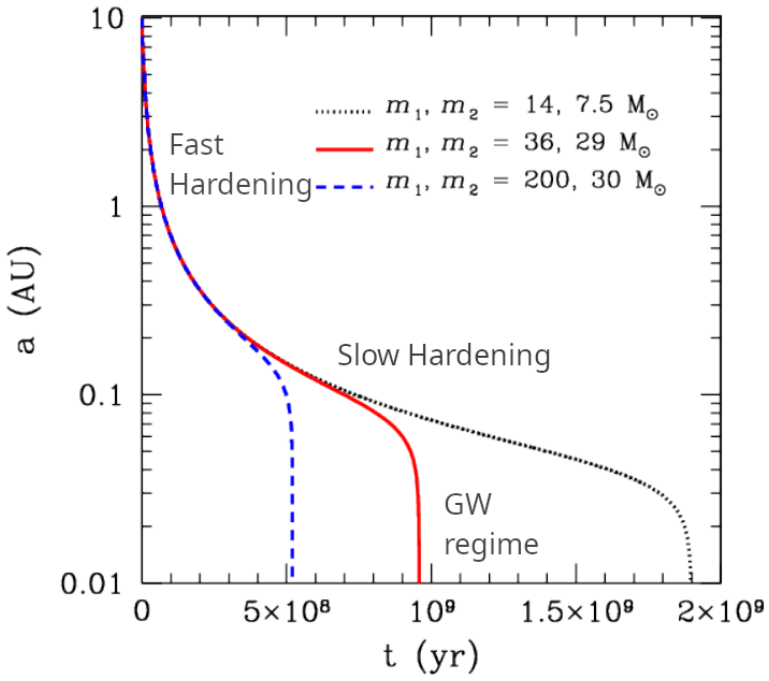

Figure 2.2: Semi-major axis time evolution caused by hardening and GW emission from Mapelli 2018 [52]. The plot shows the numerical results of equation 2.20 considering three different binaries and $\xi = 1$, $\rho = 10^5\, M_\odot$, $\sigma = 10\, km\, s^{-1}$, $e = 0$, $a_0 = 10\, AU$ (σ, ρ, e are assumed constant in time). When a is large hardening processes predominate and we are in the fast hardening regime. The more the sami-major axis gets smaller, the less efficient (eq. 2.16) and numerous (eq. 2.13) are the hardening processes. The binary enters therefore in the slow hardening regime in which a is still too wide for considerable GW emissions. Finally, when $a \leq a_{gw}$ (eq. 2.22), the binary can enter in the last regime in which the emissions of GW will lead it toward the merger.

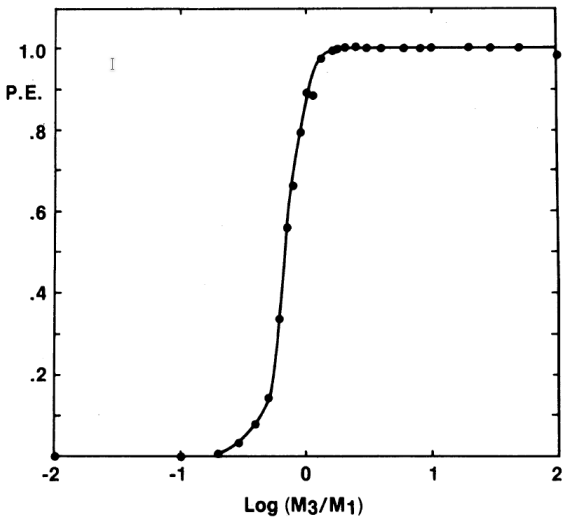

Figure 2.3: Exchange probability (P.E.) in function fo the mass ratio between the intruder object and the secondary component of the binary system (Fig.4 from Hills & Fullerton 1980 [29]). The higher is the intruder mass m_3, the more likely an exchange will happen.

encounters in which the single object replaces the less massive member of the binary system. Hills & Fullerton (1980 [29]), exploiting the analytical approach of Heggie (1975 [28]), demonstrated with numerical simulations that the probability for an exchange event in a three-body interaction between a single object and the secondary component of the binary (i.e the less massive component) is higher (~ 1) if the intruder is more massive than one of the binary members. The probability is instead lower (~ 0) if the intruder is less massive than both the components of the binary. The results of their simulations are reported in figure 2.3. Therefore, since in general the replaced component of the system is less massive (m_2) respect to the intruder m_3, we have that exchanges create binaries with higher binding energy as follow:

$$E_{b,i} = \frac{Gm_1m_2}{2a_i} < \frac{Gm_1m_3}{2a_f} = E_{b,f}. \tag{2.25}$$

Where the subscripts i and f refer respectively to the initial and final values of the BBH, before and after the three-body interaction took place.

Black holes are among the most massive objects of a star cluster, therefore they will likely undergo several exchanges to form binary systems. A star binary system can thus first experience an exchange event in which one of the two stars is replaced by a BH, and later a second exchange in which another BH takes over for the second star in the binary, giving birth to a BBH. This scenario, which is represented in figure 2.4, has been tested with

direct N-body simulations by Ziosi et al. (2014 [90]), and they reported that more than 90% of BBHs in young star clusters are formed via dynamical exchanges. As long as the new-born BBH is harbored in a dynamical active environment, its growth in mass does not stop. In fact, exchange processes can still go on even after the formation of a BBH, such that heavier black holes can still be introduced in the BBH while the lighter one is ejected. This has the result of increasing the average mass of BBHs produced by the dynamical channel with respect to the ones formed via stellar evolutions of isolated original binaries. Furthermore, several exchanges that involve a BBH with more massive black holes can lead to the formation of an IMBHB. In the next chapter (section 3.3) we will explain the key role of exchanges in the formation of IMBH via the repeated merger scenario.

Another fingerprint of dynamical formation of BBHs via exchange processes is provided by high eccentricity: dynamical captured objects tend to bind in highly eccentric orbits, favoring the production of eccentric binaries. None of the ten detections observed by LIGO/Virgo in the first two observative runs has identified an eccentric BBH merger (The LIGO/Virgo Scientific Collaboration 2020 [85]). We need therefore more observations to use e as a tool to uncover the possible dynamical origin of a BBH.

Lastly, the members of BBHs born via exchanges will likely have misaligned or nearly isotropic spins since dynamical processes tend to completely reset the values of the original spins. The opposite is true for original isolated binaries whose members may evolve in BHs via direct collapse giving birth to a BBH with nearly aligned spins. Tidal interactions and mass transfers tend, in fact, to synchronize the spins during binary evolution (Hurley et al. 2002 [32]), and even if a clear relation between the magnitudes of the progenitor-BH spins still does not exist, it is, however, reasonable to assume that the spin orientation is conserved (Mapelli 2018 [52]). The situation is trickier for original binaries that evolve in a dense environment such as star clusters because they tend to participate in the cluster dynamics, and consequently, the spins of the binary components result in moderately misalignement (one more cause of misaligned spins is provided by the natal kick if one binary component undergoes a core-collapse supernova). Unfortunately, the sample of BBH mergers observed so far (The LIGO/Virgo Scientific Collaboration 2019 [84]) have put only poor constraints in the effective spin measurements χ_{eff} (i.e. the sum of the spin components of the two BHs along the direction of the binary angular momentum vector), and there is not enough statistic to clearly constrain the BBHs formation scenario between the dynamical and the stellar evolution channels (Bouffanais et al. 2019 [7]). The only information derived by the observations made so far seems to point that there is a small preference for low-spin magnitudes respect to a high-spin magnitude population of BHs (The Ligo/Virgo Scientific Collaboration 2019 [86])

Lastly, the only event with a partial spin constraint is GW151226, which χ_{eff} measurements seems to favour aligned spins (Abbott et al. 2016 [1]).

2.2.4 Ionization

If the third star loses a fraction of its kinetic energy while the internal energy of the binary becomes more positive, the kinetic energy of the three-body center-of-mass is decreases $E_{k,i} > E_{k,f}$ and so do the binding energy of the binary $E_{b,i} > E_{b,f}$. As a consequence of the dynamical interaction with the single star, the binary semi-major axis increases $a_i < a_f$ and becomes less bound or soften. This can also cause the *ionization* of the binary, i.e. the binary components have $E_{tot} > 0$ and can be considered as single stars. For this to happen, the kinetic energy of the reduced particle in the three-body system must be equal to the binding energy of the binary

$$\frac{1}{2}\frac{m_3(m_1+m_2)}{(m_1+m_2+m_3)}v_{crit}^2 = \frac{Gm_1m_2}{2a}. \tag{2.26}$$

From this expression, it is possible to derive (Hut & Bahcall 1983)

$$v_{crit} = \sqrt{\frac{Gm_1m_2(m_1+m_2+m_3)}{m_3(m_1+m_2)a}} \tag{2.27}$$

which is the critical velocity. A single star with mass m_3 can ionize a binary system if its velocity at infinity exceeds this critical value.

2.2.5 Hierarchical Triple Systems

We define a hierarchical triple as a resonant three-body system composed of a tight binary system, often called inner binary, bound with a third body in a wider eccentric orbit, called outer binary. These kind of systems are the products of three-body encounters in which part of the intruder kinetic energy is transferred to the internal energy of the binary. This can reduce the intruder velocity enough to avoid the escape at infinity, leading the third object to bind gravitationally with the binary. Since in dynamical encounters the intruder incoming direction is isotropic respect to the binary orientation, in a hierarchical triple system the third object orbital plane is generally inclined respect to the orbital plane of the binary. Therefore, each passage of the wider object at the pericenter will induce a perturbation to the inner binary which as result will experience oscillations in the eccentricity and in the relative inclination angle of the orbital plane with the outer binary. This effect is known as the Kozai-Lidov oscillations (Kozai 1962 [38], Lidov 1962 [44]) and can have a huge impact in the coalescence time of the inner binary. This highly depends on the eccentricity of the inner system (Eq. 2.19), which can be rapidly increased by a Kozai-Lidov perturbation leading

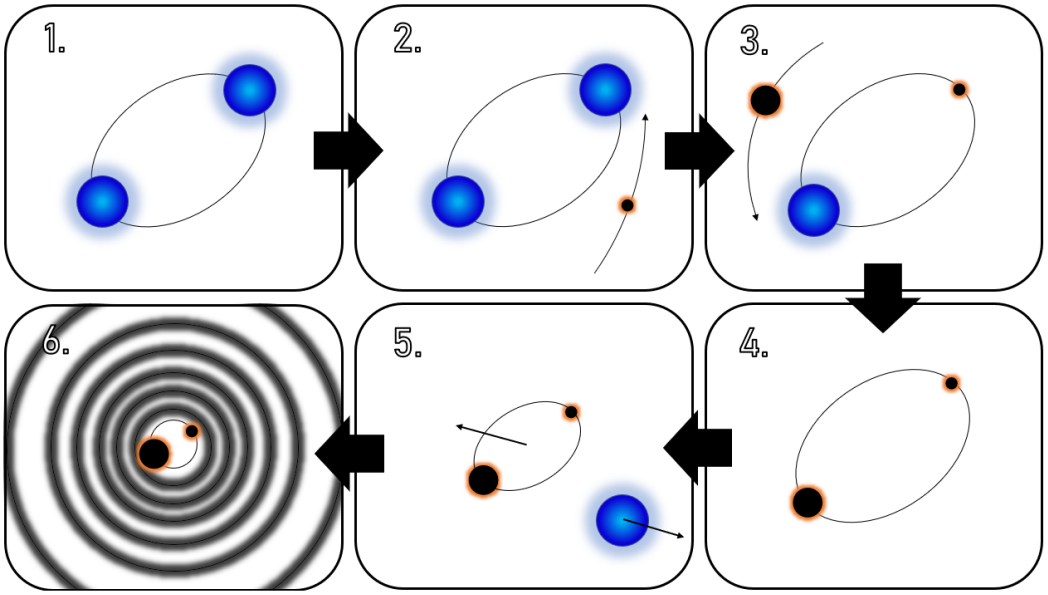

Figure 2.4: Example of BBHs dynamical formation channel. Blue dots are stars while black dots are black holes. 1 - star binary system. 2 - Three-body encounter between the binary and a black hole. If the black hole is more massive than one of the two components, it can replace the secondary star via the exchange mechanism. 3 - A second exchange replaces the other star with another black hole. 4 - A BBH formed via three-body interactions is born. 5 - Hardening processes cause a to shrink and induce a recoil. 6 - If hardening processes have been efficient enough, the BBH can enter in the gravitational wave regime and its semi-major axis keeps decreasing due to the GW emission while the orbit becomes circularized. The same scheme work if the binary system in box 1 is a BBH: in this case, the exchange processes can introduce more massive black holes in the system. If one of the two components of the BBH is replaced with an IMBH, the binary becomes an IMBHB. Lastly, if the merger product in box 6 does not experience a dynamical ejection from the cluster, it can create a second generation BBH via three-body encounters (e.g. in box 2) establishing a loop process in which a BH keeps growing in mass (repeated mergers scenario, see next chapter).

the inner binary to merge. It has been measured that in globular clusters the Kozai-Lidov mechanism could be the merger driver for $\sim 10\%$ of all the dynamically-formed BBHs (Antonini et al. [4]) while, in young star clusters and open clusters, the Kozai-Lidov resonance could increase the merger rate by $\sim 40\%$ (Kimpson et al. 2016 [37]). The mergers caused by Kozai-Lidov oscillations are produced by binaries characterized by high values of e up to the last few seconds before the merger. This feature might be measurable with the future laser interferometer space antenna LISA (Nishizawa et al. 2017 [62]) and may already be observable in the aLIGO/aVirgo frequency range (Antonini et al. 2016 [4]). If such detection with high eccentricity were measured, it would better constrain the role of dynamics in the evolution of BBHs and the production of massive black holes.

Chapter 3

IMBHs Formation

Several studies (Heager et al. 2003 [27], Portegies Zwart & McMillan, 2002 [66] and 2010 [68], Mapelli et al. 2013 [50], Mapelli 2016 [51], Spera & Mapelli 2017 [78], Di Carlo et al. 2019 [16]) show that the formation of intermediate-mass black holes (IMBHs) requires two main ingredients: low metallicity and dynamics. Low metallicity is intrinsically linked with the mass loss caused by wind emission in the main sequence phase of the progenitor stars, and is therefore directly related to the final mass in the pre-supernova phase. Dynamics enhances the probability of close encounters and thus provides a machinery that increases the chances for collisions, which can possibly give birth to massive compact objects. In this chapter, we are going to summarize in detail the most important processes that can lead to the formation of an IMBH in a young dense star cluster.

3.1 Direct Collapse

The total mass of a stellar-origin black hole is strictly related to two main processes that its stellar progenitor experiences during its lifetime. On the one hand stellar winds drive are the main driver of mass loss and reduce the final mass of the star, on the other hand, the final supernova explosion (or direct collapse) determins the mass of the compact object. In this section, we are going to resume these two mechanisms, in order to finally present the possible progenitors for IMBHs and their main characteristics.

3.1.1 Stellar winds

Throughout their life, stars experience mass loss episodes under the form of stellar winds, which are outflows of gas ejected from the upper atmosphere of a star. Stellar winds drastically decrease the initial mass of the star along its evolutionary path, and their nature depends on the star type. For evolved

cold stars (e.g. red giants, asymptotic giant branch stars) winds are produced by the interaction between radiation pressure and dust particles in the colder outer layers of the atmosphere, while in massive hot stars (e.g. O, B, Wolf-Rayet, Luminous Blue Variables), winds are driven by radiation pressure on the resonance absorption lines of atmospherical metal ions. Massive stars winds, and the relative mass loss rate $\dot{m}$, are therefore strictly related to the star metallicity Z. For O-B stars, this dependence can be expressed with the relation found by Vink et al. (2001 [89]):

$$\dot{m} \propto Z^{0.85} v_{\infty}^{p} \qquad \begin{cases} p = -1.23 & if \quad T_{eff} \gtrsim 25000K \\ p = -1.60 & if \quad 12000K \lesssim T_{eff} \lesssim 250000K \end{cases} \tag{3.1}$$

where T_{eff} is the effective temperature of the star and v_{∞} is the terminal velocity of the wind which corresponds to its maximum velocity. For Wolf-Rayet stars, exists a similar expression (Tang et al. 2014 [81], Chen et al. 2015 [14]) that keeps account also of the Eddington factor Γ_{Edd}:

$$\dot{m} \propto Z^{\alpha} \qquad \begin{cases} \alpha = 0.85 & if \quad \Gamma_{Edd} < 2/3 \\ \alpha = 2.45 - 2.4\Gamma_{Edd} & if \quad 2/3 \leq \Gamma_{Edd} \leq 1 \end{cases} \tag{3.2}$$

The Eddington factor is defined as the ratio between the star luminosity and the Eddington luminosity $L_{Edd} = 4\pi cGM/k$, i.e. the maximum luminosity for a star in hydrostatical equilibrium given its mass M and the electron-scattering cross section k.
Therefore for massive stars we have that the higher the metallicity, the higher is the mass lost by wind emissions while the star evolves, and the lower the remnant mass left after the star has died.

3.1.2 Supernova Mechanisms

A second and even more important constraint on the mass, or even the existence, of a compact remnant is the supernova mechanism that concludes the star life.

Stars with zero-age main sequence mass (m_{ZAMS}) in the range $8 \lesssim m_{ZAMS}/M_{\odot} \lesssim 30$ experience a core-collapse supernova. In the last stages of these stars, energy can no longer be produced by fusion, electrons are captured by inverse beta-decay to produce neutrons and neutrinos while the degenerate Iron-Nickel core collapses when it reaches the Chandrasekhar mass limit ($\sim 1.4\, M_{\odot}$). This causes an outgoing bounce shock that reverses the supersonic infalling material of the outer envelopes. Neutrino Energy possibly contributes to the reverse blastwave, which leads the outer layers of

the star to explode. Since part of the total mass is ejected in the explosion, core-collapse SNe produce low-mass compact objects such as neutron stars or stellar-mass black holes in the range $\sim 3-15\,M_\odot$ (Fryer 1999 [19]). In some cases, neutrinos energy contribution is not sufficient to re-ignite the outgoing blastwave, and the shock stalls leading a great part of the star layers to fall and accrete the proto-neutron star. If degeneracy neutron pressure is not sufficient to overcome the infalling material pressure, the proto-neutron star can become a black hole by fallback with slightly higher masses in the range $\sim 15-30\,M_\odot$[1].

More massive stars $m_{ZAMS} \gtrsim 30\,M_\odot$ can build up a Carbon-Oxygen core of $m_{CO} > 7.6\,M_\odot$ ending their life via the direct collapse mechanism to form a BH with $m_{BH} \geq 20\,M_\odot$ (Fryer et al. 2012 [20]). Direct collapse SNe are failed supernovae and differ from the core-collapse mechanism because the outgoing shock wave generated by the core contraction fails to unbind mass, therefore all the star envelopes keep falling and no ejecta are produced. All the mass is accreted by the central compact object, and if the pre-SN star is massive enough an IMBH can be left. Furthermore, due to the nearly spherical symmetry of the process, kick velocities are highly reduced with respect to the core-collapse case. However, for stars with mass $\gtrsim 30\,M_\odot$, winds start to become the main mass loss process that affects the mass of the remnant (Mapelli 2018 [52]). Therefore, a massive CO-core can be developed only by massive stars for which winds losses are relatively low-efficient, or in other words, by stars with low metallicity $Z < 0.1\,Z_\odot$ and Eddington factor $\Gamma_{Edd} < 0.6$. When $Z \sim Z_\odot$ or $\Gamma_{Edd} > 0.6$, stars are instead subjected to massive stellar winds, and the CO-core cannot grow above the threshold leading the star to explode as core-collapse SN with the production of a lower mass BH.

One more outcome is given for stars with Helium core grown up to $m_{He,f} \sim 30\,M_\odot$. In this case, pair production becomes extremely efficient in the core, and the electron-positron pairs make Oxygen/Silicon to ignite in a thermal runaway reaction which exerts a pulse outwards. This process can repeat several times and, if the star is able to restore the equilibrium after these instabilities, the phenomenon is defined as a pulsational pair-instability SN (PPISN). This induces severe mass losses to the star, which will eventually end its life by core-collapse leaving a lighter black hole $m_{BH} \sim 30-55\,M_\odot$ respect to the expected values of $m_{BH} \sim 50-100\,M_\odot$ without pulsations. On the other hand, if the star cannot survive to this

[1] The mass ranges in which a supernova gives birth to a neutron star by core-collapse or a black hole by fallback are still matter of discussion. O'Connor & Ott [63], for example, proposed an "island of explodability" scenario derived from their 1D hydrodynamical simulations in which SN explosion mechanisms do not behave monotonically with the mass of the progenitor star.

explosive burning phase, it explodes in a pair-instability supernova (PISN) leaving no remnant. PISNe and PPISNe cause the pair-instability mass gap in the range $60 \lesssim m_{BH}/M_\odot \lesssim 120$, in which no black holes are expected to be formed by a single star.
Recent numerical simulations performed by Woosley (2017 [93]) explored the evolution of metal-poor ($Z \simeq 0.1\, Z_\odot$) and Helium-only stars, to better constrain the mass ranges of the progenitor stars that produce the pair-instability mass gap. He found that if $70 \lesssim m_{ZAMS}/M_\odot \lesssim 150$ (i.e. $32 \lesssim m_{He,f}/M_\odot \lesssim 64$) a star may undergo a PPISNe while if $150 \lesssim m_{ZAMS}/M_\odot \lesssim 260$ (i.e. $64 \lesssim m_{He,f}/M_\odot \lesssim 135$) a star can explode by PISN.
Moreover, Spera & Mapelli (2017 [78]) studied the effects of PISNe and PPISNe on the black holes mass spectrum at different metallicities. They found that at metallicities of $Z \lesssim 0.1\, Z_\odot$, stars in the $60 - 125\, M_\odot$ ZAMS mass range can experience PPISNe, while PISNe become effective when stars with metallicities $0.05 \lesssim Z/Z_\odot \lesssim 0.4$ have $150 \leq m_{ZAMS}/M_\odot \leq 350$ (the lower limit is slightly depends on Z). They report that PISNe and PPISNe, besides preventing the formation of BHs in the $60 - 120\, M_\odot$ range, tend also to enhance the formation of BHs with $30 - 50\, M_\odot$ for low metallicity values. Even if at lower values of Z the pair production effects in the star evolution are less significant, they conclude that metal-rich stars ($Z \geq 10^{-3}$) cannot produce IMBHs due to the line-driven winds experienced along the stars lifetime. On the other hand, massive stars and metal-poor stars with $m_{ZAMS} \gtrsim 200\, M_\odot$ and $Z \lesssim 0.07\, Z_\odot$ can avoid PISNe and produce intermediate-mass black holes by direct collapse. These results are reported in Fig.3.1, which compares supernova models with and without the effects of PISNe and PPISe at different values of Z. From the plot, it is visible that not only pair-instability highly affects the remnant mass spectrum, but it also strongly depends on the metallicity of the progenitor star.

From the above theoretical results we can infer that ideal progenitors for IMBHs are massive $m_{ZAMS} \gtrsim 260\, M_\odot$ metal-poor $Z \lesssim 0.07\, Z_\odot$ stars for which wind-driven mass loss has been negligible along the star lifetime. These characteristics allow the star to avoid a PISN-fate, which instead experiences a direct collapse forming an IMBH. Following this logic, two main candidates as progenitors have been proposed:

- Population III stars are the hypothetical first generation of stars that formed in the early ages of the universe. Characterised by zero-metallicity and thus nearly zero mass loss (Wise 2012 [92]), these objects represent a good candidate as progenitors of massive black holes (Madau & Rees 2001 [46], Whalen & Fryer 2012 [91]). The plot in figure 3.3 shows the mass spectrum of the remnant against the mass of the progenitor

(Heger et al. 2003 [27]), and summarizes all the possible SN outcomes reviewed above for a zero-metallicity star. By comparison, in Fig.3.2 it is reported the same plot but for $Z = Z_{\odot}$, which highlights the differences given by metallicity between a population III and a solar-metallicity star. The problem of Population III stars is that they can be possibly form just at high redshift values ($z \sim 6$), and this limits the production of IMBHs from pop III stars in the first few Myr of the Universe.

- The solution to this last problem is provided by another family of potential candidates as IMBHs progenitors. These are the very massive stars (VMS), i.e. stars with $m_{ZAMS} \gtrsim 100 M_{\odot}$ (Zwart & McMillan 2002 [66], Zwart et al. 2004 [67], Freitag et al. 2006 [18]). In contrast to population III stars, VMSs are possibly[2] still formed in the core of dense star clusters by runaway collisions (see next section 3.2). VMSs can be massive enough to avoid PISNe ($m_{ZAMS} \gtrsim 200 M_{\odot}$) and direct collapse to form a black hole with $m_{BH} \geq 100 M_{\odot}$.

3.2 Runaway Collisions

Firstly proposed more than fifty years ago by Colgate (1967 [15]) and Sanders (1970 [74]), this theory explores the consequences of clusters dynamics and mass segregation which can possibly lead to the formation of an intermediate-mass black hole. Star clusters are self-gravitating particle systems whose evolution is dominated by two-body relaxation. Since gravity is a long-range force, all the stars in a cluster are mutually subjected to the gravitational force exerted by any other star. This cumulative effect, known as two-body relaxation, induce all the star velocities to change in direction and magnitude. We can thus define the two-body relaxation timescale as the time needed for a star with mass m to completely lose memory of its initial velocity as an effect of several two-body interactions. We can now resume equation 2.3, and rewrite it in a more accurate form that keeps account of the diffusion coefficients (Spitzer 1971 [80]) to define the relaxation timescale as

$$t_{rlx} = 0.34 \frac{\sigma^3}{G^2 \langle m \rangle \rho \ln \Lambda} \tag{3.3}$$

[2]The most massive stars observed in the local universe are located in the ionizing star cluster 30 Doradus in the Large Magellanic Cloud, and have masses of $m > 150\, M_{\odot}$ (Crowther et al. 2016 [13]) derived with evolutionary models. It is important to notice that 30 Doradus present a metallicity of $\sim \frac{1}{3} Z_{\odot}$ (Geha et al. 1998 [22]), which can still cause severe wind emissions and therefore heavily impact the evolution of these massive stars.

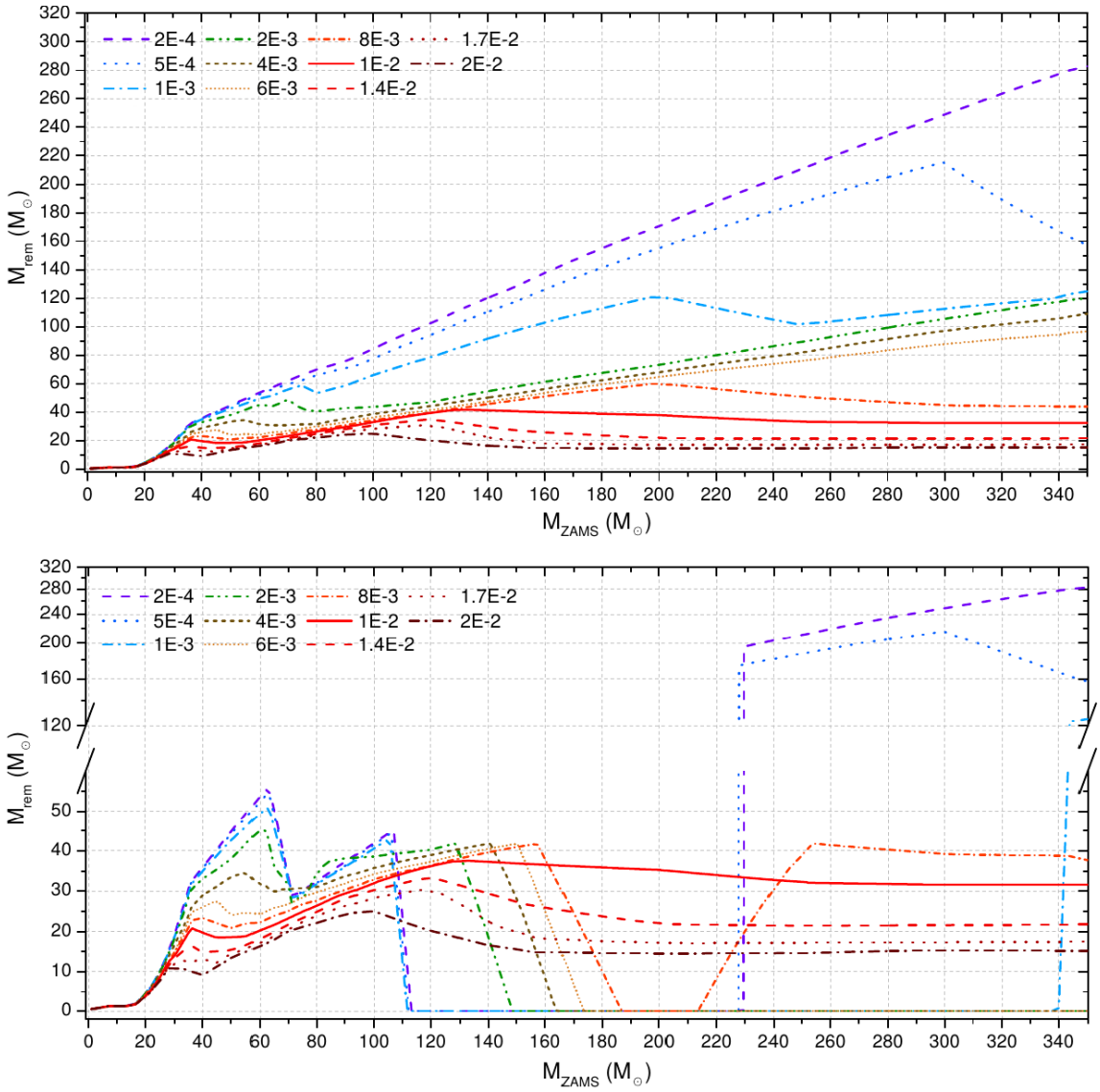

Figure 3.1: Mass of the remnant vs zero age main sequence mass (m_{ZAMS}) of the progenitor star from Spera & Mapelli (2017 [78]) with (below) and without (top) considering the PISNe and PPISNe. The y-axis of the bottom plot is broken in the range $60 \lesssim m_{rem}/M_{\odot} \lesssim 120$ due to the lack of black holes caused by PISNe and PPSNe (pair-intability mass gap). The plot shows that only stars with low value of Z can experience pair instability, while, on the other hand, are the only ones to cause IMBH formation by direct collapse.

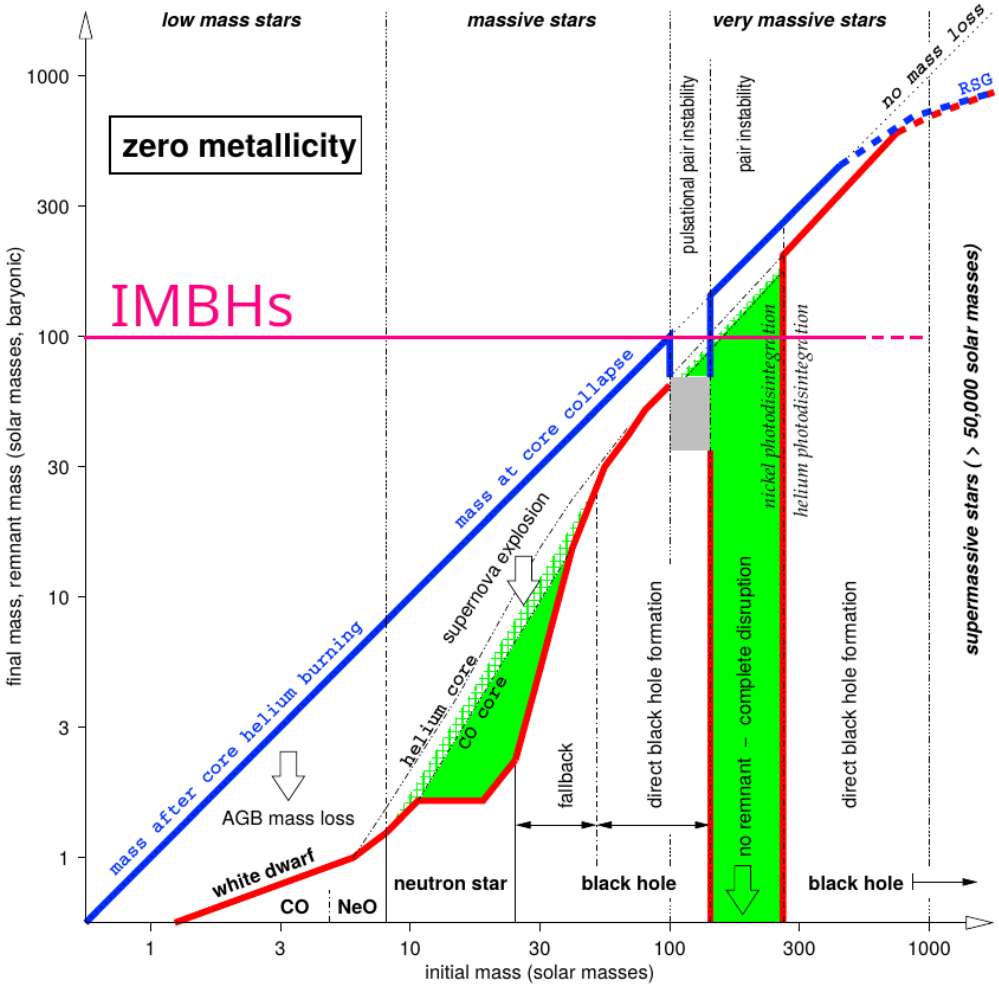

Figure 3.2: Adaptation of Fig.3 from Heger et al. 2003 [27]. Zero Age Main Sequence (ZAMS) mass of a non-rotating, zero-metallicity star (x-axis) vs final (pre-SN) mass of the same star after stellar evolution (y-axis, blue curve) and remnant mass (y-axis, red curve). The pink horizontal line shows the limit above which a BH can be considered IMBH, and it highlights that only massive stars ($\gtrsim 260 M_{\odot}$) that avoid pair-instability can produce a $m_{BH} \geq 100 M_{\odot}$ through the direct collapse mechanism. Notice in green the pair-instability mass gap $140 \lesssim m_{ZAMS}/M_{\odot} \lesssim 260$, in which stars are disrupted by a single pulse generated by explosive thermonuclear reactions. The PPISN range is instead $100 \lesssim m_{ZAMS}/M_{\odot} \lesssim 140$. The rest of the plot shows prescriptions for other SNe mechanisms in the low mass and massive star range.

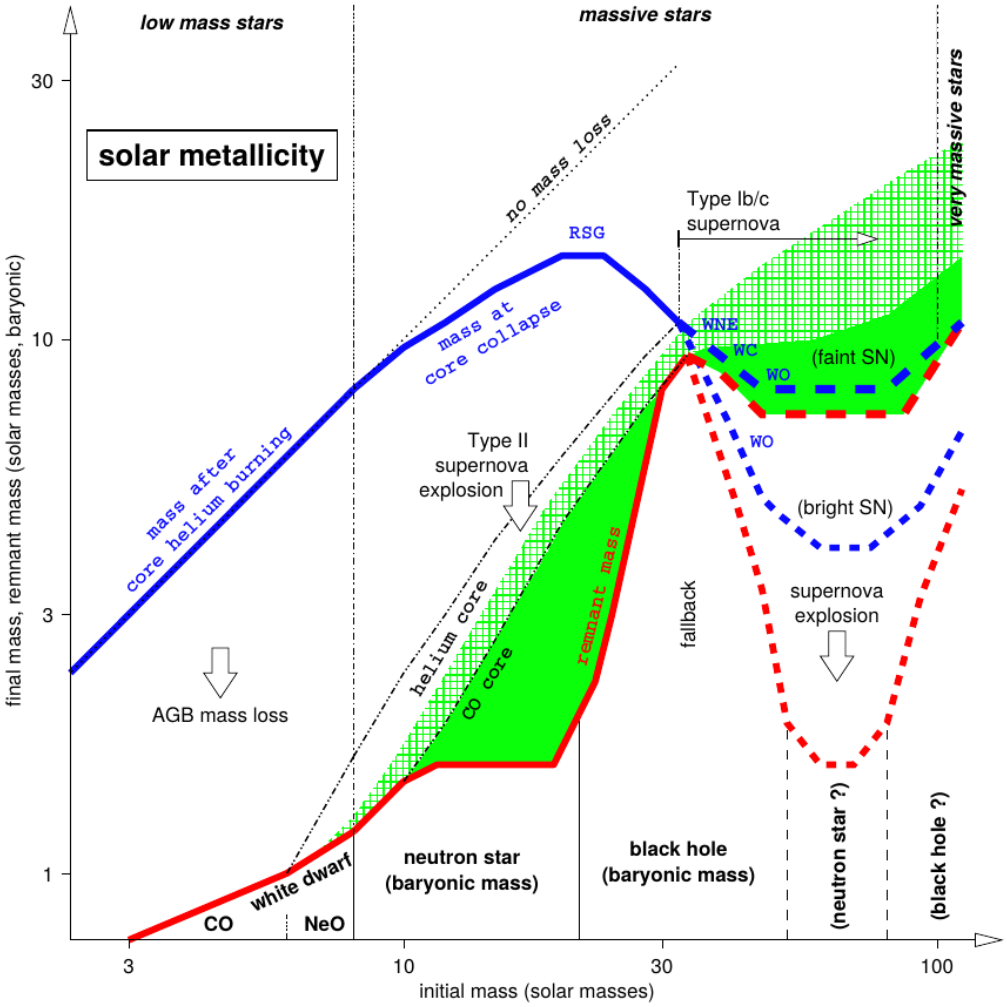

Figure 3.3: Same plot as of Fig.3.3 but for $Z = Z_{\odot}$ taken from Heger et al. 2003 [27]. At these levels of metallicity stars can avoid PISNe and PPISNe, and no pair-instability gap is formed. Even so, mass losses caused by stellar winds become extremely high at solar metallicity, therefore the mass of the compact object is heavily reduced and no IMBH can be formed (this is clearly visible comparing the y-axis of this plot with the y-axis of Fig.3.3).

where σ is the velocity dispersion of the system, $\langle m \rangle$ the average particle mass, $\Lambda \sim N$ number particles of the system and $\rho \propto N\,m/R^3$ with R radius of the system. The expression can be rewritten in a more practical form (Zwart & McMillan, 2010 [68]) in function of measurable quantities as follow

$$t_{rlx} \simeq 20\ Myr \left(\frac{R_{cl}}{1pc}\right)^{3/2} \left(\frac{M_{cl}}{10^4 M_\odot}\right)^{1/2} \left(\frac{\langle m \rangle}{1 M_\odot}\right)^{-1} \tag{3.4}$$

where M_{cl}, R_{cl} and $\langle m \rangle$ are respectively the total mass, the viral radius and the average star mass of the cluster.
Two-body interactions are extremely important also to define another effect. The most massive stars of a cluster are in fact decelerated due to the gravitational drag force exerted by the lighter objects in their surroundings. This effect is called dynamical friction, and lead all the massive objects to sink toward the center of the cluster potential well in a process known as mass segregation. It is possible to define (Chandrasekhar 1943 [9]) the typical timescale that a star with mass m takes to drift to the center of the cluster because of dynamical friction (dynamical friction timescale) as

$$t_{df} = \frac{3}{4(2\pi)^{1/2} G^2 \ln \Lambda} \frac{\sigma^3(r)}{m \rho(r)}. \tag{3.5}$$

Finally, since two-body relaxation and dynamical friction are two sides of the same coin, it is possible to combine this last equation with 3.3 to find an expression that relates the two quantities

$$t_{df}(m) = \frac{\langle m \rangle}{m} t_{rlx}. \tag{3.6}$$

The question is now if these massive stars can reach the cluster core within their lifetime, i.e. if $t_{df} < t_{lifetime}$. A stars with $m \geq 25 M_\odot$ can live approximately for $t_{lifetime} \sim 2.5\ Myr$. If we assume a cluster with $M_{cl} = 10^4\, M_\odot$, $R_{cl} = 1\, pc$ and $\langle m \rangle = 1\, M_\odot$, we have that $t_{df} \leq 1\ Myr$ (Mapelli 2018 [52]), and the star can drift to the center of the luster within its lifetime. As a rule of thumb, runaway growth can be experienced by a cluster only if the lifetimes for the most massive stars exceed the dynamical friction timescale in which they segregate. Therefore, the core can be populated by the most massive stars of the cluster, and the density of this region is extremely increased, while the probability of collisions is highly boosted up. If this happens, the most massive star in the cluster core dominates the collision rate. It increases its mass through mergers with other stars, making more likely other interactions and mergers, and less likely to escape from the cluster (Portegies Zwart and McMillan, 2002 [66]). Hence, the majority of collisions involve one particular object, most likely a star in a binary system (due to the higher cross-section), which is the product

of the first dynamical collision process and it is denoted as the principal collision product (Mapelli 2016, [51]). It is probable, therefore, that the principal collision product will participate in subsequent collisions, mostly with other binary stars. This leads to a runaway process that, according to several numerical studies (Portegies Zwart et al. 1999 [65], Portegies Zwart & McMillan 2002 [66], Portegies Zwart et al. 2004 [67], Mapelli 2016 [51]), results in a formation of a $\gg 100 M_{\odot}$ very massive star that can grow up to 0.1% of the total mass of the cluster in about 0.2 t_{rlx} but no longer than 5 Myr, after a number of collisions that is dependent on stellar winds and cluster's core density. These very massive stars are indeed good candidates to become IMBHs by direct collapse, but their fate strongly depends on their final mass. The latter is highly affected by the mass lost in each collisional process and it suffers the effects of the stellar winds experienced by the massive star. Furthermore, it does not depend on the collision number and the time of the first collision (Mapelli 2016 [51]).
In particular, hydrodynamical simulations have shown that up to $\sim 25\%$ of the merger product mass can be ejected in the collision processes between massive stars (Gaburov et al. 2010 [21]), while if the merging systems is a star-black hole system, only $\sim 50\%$ of the star mass can be directly accreted by the BH[3] (Ramirez-Ruiz & Rosswog 2009 [70]).
On the other hand, metallicity plays a key role in the evolution of these massive runaway object, because it is strictly related to stellar wind. Since massive stars are radiation pressure dominated, stellar winds at high values of Z can have a huge impact on the formation of a massive compact object. In a recent work, Mapelli (2016 [51]) found in her simulations that at solar metallicity ($Z_{\odot} \simeq 0,02$) no IMBHs can form from runaway collision in young dense star clusters. Contrarily, at $Z \leq 0.1\, Z_{\odot}$, $10 - 20\%$ circa of the principal collision products form IMBHs with masses up to $250\, M_{\odot}$, three of which are bounded in black hole binary systems which can be considered IMBH Binaries[4]. Runaway collision is, therefore, an efficient process for the production of IMBHs in young dense star clusters (Portegies Zwart et al. 2004 [67], Mapelli 2016 [51]).

[3]This value is still debated in literature. Nevertheless, Giersz et al. (2015 [23]) found that for accretion of only $\sim 25\%$, IMBHs can still be created. Because of the smaller mass accretion rate, the timescales are larger and the maximum mass lower respect to the $\sim 50\%$ case: check image 19 of the paper for further details.

[4]It is important to notice that these results come from simulations that do not include prescriptions for PPISNe and PISNe. Spera & Mapelli (2017, [78]) have revisited the evolution of the same PCPs including PPISNe and PISNe, and they found that the percent of runaway product that forms IMBHs in metal-poor star cluster is enhanced to $20 - 30\%$.

3.3 Repeated Mergers

In the last paragraph we have seen that if the dynamical timescale is shorter than the lifetime of the most massive stars of the cluster, these can migrate toward the cluster's core and trigger a runaway process that can yield to an IMBH birth. But what if these stars die before reaching the center of the cluster (*i.e.* if $t_{lifetime} < t_{df}$)? They would likely end their life leaving a compact object more massive than the average star mass $\langle m \rangle$ of the cluster. This remnant would keep sinking in the cluster core where the density is higher, proceeding even faster if bounded in a binary system. If the remnant is a black hole, it has high chances to find a massive companion and form a BBH system, which can subsequently interact repetitively with other black holes and cause repeated mergers. This possibility has been first proposed by Miller & Hamilton (2002 [61]) to explain an alternative scenario for IMBH formation. The idea can be summarized as follow:

I. Dynamical formation of a black hole binary, which is most probably a hard binary (Mapelli 2018 [52]).

II. The BBH is hardened by three-body interactions and its semi-major axis gets shrunk.

III. Due to the hardening process (check section 2.2), the binary can enter the gravitational wave regime which further reduces the orbital separation because of gravitational wave emission. This will eventually lead to the merger of the two black holes.

IV. The merger product is a massive black hole, therefore, if relativistic kick has not expelled it from the cluster, it will probably find a new massive companion. If the secondary object of the new-born binary system is a black hole, we are again in the situation of the point I.

This loop can go on several times until the main black hole becomes an IMBH, but this process presents different complications that need to be discussed.

First, the hardening process induces a recoil on the BBH when this interacts with a third object. This recoil can be strong enough to eject the binary from the cluster before further hardening interactions tighten its orbit in the gravitational radiation regime (Sigurdsson & Hernquist 1993 [75]). It has been proved (Miller & Hamilton 2002, [61]) that exists a maximum binding energy $E_{b,min}$ (i.e. a minimum semi-major axis a_{crit}) above (below) which the binary is expelled from the cluster after a three-body interaction. From the same calculations, assuming a cluster with $v_{esc} \simeq 50\,km\,s^{-1}$, it follows that a black hole with $M \geq 50 M_{\odot}$ has enough inertia to remain bound to the cluster after the recoil, while all the lighter ones may be ejected. This result

puts an important constraint in the probable minimum mass for black holes that participate to the repeated merger mechanism for the formation of an IMBH. Actually, Quinlan (1996 [69]) has shown that if in a three-body interaction the binary mass ratio m_1/m_2 is high, the hardening process increases the eccentricity while the orbit shrink, and this translates in a reduction of a_{crit} which can allow lower-mass black holes to grow by mergers avoiding a cluster ejection (Miller & Hamilton 2002 [61]). Therefore, small mass black holes may be still in the game for IMBH formation via repeated merger, since they can avoid strong hardening recoil as long as they belong to highly eccentric systems.

Second, one may wonder why black holes would more likely interact with other black holes to form a BBH system, and less likely with other core objects. Naturally, the rate of encounters in the core is strictly related to the density of field black holes. In particular, under thermal equilibrium, binary encounters with single stars are dominated by the most massive objects of the cluster, which in general are black holes (Sigurdsson & Phinney 1995 [77]). Therefore, BH-star binary systems will likely interact with other black holes, which will probably take over for the star via dynamical ejection forming a BBH. This explanation holds if interactions involve binary systems, because of their high cross-section. But what about single black holes? Miller & Hamilton [61] have shown that if thermal equilibrium holds, the slowest moving population dominates the encounter rate, and this means black holes. Therefore black holes have high chances in a dynamically active and dense environment to find a similar partner.

Third, the most important issue is related to the relativistic kick received by the product of a gravitational wave merger due to the anisotropic gravitational wave emission. This post-merger kick can lead the new-born black hole to recoil with velocities up to thousand of $km\,s^{-1}$ (Lousto & Zlochower 2009 [45]). Holley-Bockelmann et al. (2009 [31]) estimated in their models that a globular cluster can retain an IMBH 33% of the times if it is assumed a Kroupa initial mass function for BHs (Kroupa 2001 [40]). Furthermore, they also show that only 16% of the Milky Way globular clusters can keep an IMBH with mass $M \geq 1000 M_{\odot}$. For a denser stellar environment such as nuclear star cluster, the escape velocity could be much higher and retention may instead be more possible. Therefore, if our loop breaks at point III because of this recoil, repeated mergers won't give birth to an IMBH.

Lastly, Giersz et al. (2015 [23] found with Monte Carlo simulations that repeated merger scenario is working in globular clusters, but it is less timescale efficient respect to other formation paths. They report in fact that both runaway collisions and repeated mergers are actively working in IMBH production, but while the first mechanism can produce massive black holes in the early ages of the clusters (few Myr, see section 3.2), the latter sets on after $\gtrsim 5 Gyr$. This implies that repeated mergers can still be working in older star clusters such as globular clusters. However, these simulations

do not consider gravitational wave recoils, and as we have already discussed, this can have severe consequences in IMBH formation.

Despite the aspects discussed above, the repeated mergers mechanism is still a prominent formation path for IMBH. Moreover, respect to runaway merger and direct collapse scenarios, it can be described just exploiting the dynamics of the cluster, without considering stellar evolution. So far, this is the only IMBH formation mechanism potentially observable with the current gravitational wave detectors despite, by now, no IMBH has been detected by aLIGO/aVirgo observatories (The LIGO Scientific Collaboration & the Virgo Collaboration 2019 [84, 2]). On the other hand, among the ten BBH mergers confirmed events, GW170729 represents the most massive system detected with a final mass of $79.5^{+14.7}_{-10.5} M_{\odot}$. Notwithstanding the low evidence that this event is a second-generation merger (Chatziioannou et al. 2019 [11], Kimball, et al. 2020 [36]), GW170729 has confirmed that the pair-instability mass gap can be filled by BHs mergers. Future observations of BBHs mergers with a mass ratio much different from one will represent an important fingerprint of BBHs dynamical formation and repeated merger scenario.

Chapter 4

Three-Body Simulations

We have seen that three-body interactions drive the dynamical encounters in dense star clusters and that they are a fundamental tool for the formation of IMBHs and IMBHBs. For these reasons, we aim to recreate a statistical sample of the three-body interactions between BBHs and massive black holes, with the goal of exploring all the possible outcomes. This chapter is thus divided into two sections: the first describes the N-body codes, their main characteristics and the code we used to recreate our mock three-body encounters, while the second section is focused on all the initial conditions assumed for these simulations

4.1 N-body codes

The N-body problem is modernly explored with the usage of the N-body codes, whose application can range from the study of few body interactions (e.g. solar system simulations) up to a huge number of particles per simulation for star clusters or even cosmology. The work of an N-body code is to solve the equations of motion of all the N particle that compose a system. If the system is a star cluster, the equation of motion for a particle i subjcted to the gravitational force of all the other particles with mass m_j is the Newton's equation of motion and can be written as

$$\vec{a}_i = -G \sum_{i \neq j}^{N} m_j \frac{\vec{r}_i - \vec{r}_j}{|\vec{r}_i - \vec{r}_j|^3} \tag{4.1}$$

With $\vec{r}_{i,j}$ the positions of the two particles. Despite being an extraordinary tool to study dynamics, N-body codes suffer several limitations that increase the computational cost of N-body simulations. In function of the solution to this problem, we can divide the N-body codes in two different categories: *direct* N-body codes and *Tree* N-body codes.

In direct gravitational N-body simulations the equations of motion of

a system with N particles under the influence of their mutual gravitational forces are integrated numerically without any simplication or approximation. The codes that perform this kind of simulations are called *direct* N-body codes, and achieve high accuracy at the price of a large computational time. The integrations are in general performed by a fourth order Hermite integrator, and are recursively repeated after an adaptive timestep that depends on the type of dynamical interaction that the program is simulating. Since accelerations are determined by summing all the pairwise interactions for the N particles, the computational time per timestep must increase as N^2, leading numerous particle systems in being extremely time-consuming to simulate.

Another family of N-body codes that solve this problem consists of those that instead of the direct integration exploit the faster *tree-algorithm* (Barnes-Hut algorithm, 1986 [6]). These codes reduce the total computational timescale, such as it scales as $N \log N$, but reduce the precision since strong interactions are typically softened and long-range interaction are approximated. Thus, direct codes are in general used in small-scale encounters in which few bodies are involved (collisional systems), while codes based on the tree-algorithm are exploited for large-scale systems (collisionless systems) in which N is high.

One more problem of the N-body codes is connected with the geometrical nature of the gravitational acceleration to scale as the inverse square of the distance. In a strong gravitational encounter between two objects, the mutual distance tends to zero leading the code to a singularity. Since the adaptive timestep for an N-body code scales as $\Delta t \propto r_{ij}^{\alpha}$ with $\alpha > 0$ and r the mutual distance between two particles, we have that for $r_{ij} \to 0$ the number of steps becomes infinitely high and this causes a large numerical error on the integration. To avoid this problem there are two solutions. One is the *softening*, which consists into adding a constant to the spatial term at the denominator of the acceleration, such as

$$\vec{a}_i = -\sum_{i \neq j}^{N} \frac{G m_j \vec{r}_{ij}}{(r_{ji}^2 + \epsilon^2)^{3/2}} \tag{4.2}$$

with ϵ the softening constant, in general defined as the radius of the star. The softening method allows to avoid rounding errors from the integration when the mutual distance between particles drastically decreases. A second and more precise method to avoid the singularity is instead the *regularization*. The regularization method consists in a change of coordinates $dt = r\, ds$ that removes the singularity, where dt is the physical time, r is the relative distance and ds is the time in the new "regularized" frame. It was first introduced by Levi Civita in 1920 ([43]) in two-dimesions to describe the Keplerian motion of two orbiting bodies as an harmonic oscillator, and it has been later generalized by Kustaanheimo and Stiefel in 1965 ([41]) in three-dimensions. Finally, it has been extended to N-body encounters by Mikkola

and Aarseth in 1990 ([56]) and implemented in N-body codes in 1993 ([57]) via the chained variables method, in which the coordinate change is

$$dt = \frac{ds}{U(r_{ij})} \qquad U(r_{ij}) = \sum_{i<j}^{N} \frac{m_j m_i}{r_{ij}} \tag{4.3}$$

with $U(r_{ij})$ the N-body gravitational potential.

4.1.1 The ARWV Code

To compute our three-body simulations we exploited **ARWV**, a Fortran direct few-body code that exploits Mikkola's algorithm for regularization (Chassonnery et al. 2019 [10]). This code integrates the few-body problem ($N \leq 500$) with high precision, making usage of the chained variables method for the coordinates and velocities of the stellar bodies. In particular, since we are interested in three-body interactions between BBHs and single massive black holes, we exploited the possibility of ARWV to compute the accelerations with a post-Newtonian approximation up to 2.5 order. The post-Newtonian approximation is extremely important since it keeps account of the dissipative term in the equations of motion caused by the gravitational wave radiation; for further informations see appendix B. The regularization in our simulations has been performed by ARWV in order to optimize the close encounters with a combination of the *logarithmic-Hamiltonian* (or the logH method, Mikkola & Tanikawa 1999 [58]) and the *Time-Transformed-Leapfrog* methods (Mikkola & Aarseth 2002 [59]). With an adaptive timestep, ARWV is capable of keeping track of the orbital evolution of all the binary systems that form, evolve and potentially merge during the simulations. The code detects a merger between an object and a black hole when the mutual distance d is equal to the innermost stable circular orbit of the black hole, i.e. $r_{ISCO} = 6Gm_{bh}/c^2$.

For each simulation, ARWV accepts as input data the masses of each particle plus the positions and velocities rescaled in the three-body center-of-mass frame. In our simulations, space, time and masses are physically measured in pc, $days$ and $M_\odot$ with $G = 3.372743 \times 10^{-20}\, pc^3 M_\odot^{-1} days^{-2}$. N-body codes run more smoothly if the physical quantities are rescaled in a reference frame in which the universal gravitational constant is one. Therefore, we first fixed the spatial and mass scale parameters to rescale the coordinates with

$$\begin{aligned} x_{code} &= x_{phys} \cdot x_{scale} = \frac{x_{phys}}{1\, pc} \\ m_{code} &= m_{phys} \cdot m_{scale} = \frac{m_{phys}}{1\, M_\odot}. \end{aligned} \tag{4.4}$$

We then derived the time and velocity scaling factors, with which we rescaled also the time and velocities as follow

$$\begin{aligned} t_{code} &= t_{phys} \cdot t_{scale} = \frac{t_{phys}}{\left[\left(\frac{1}{x_{scale}}\right)^3 / \left(\frac{G}{m_{scale}}\right)\right]^{1/2}} \\ v_{code} &= v_{phys} \cdot v_{scale} = v_{phys} \cdot \frac{x_{scale}}{t_{scale}}. \end{aligned} \tag{4.5}$$

Once performed this rescaling procedure, all the input conditions are set in a frame where calculations can be carried on with $G = 1$.

Lastly, ARWV implements a merging routine that computes the relativistic recoil velocity of the merger remnant, whose position is located in the center-of-mass of the previous pair. This relativistic kick is a consequence of the fact that BBHs radiate anistropic gravitational radiation. This causes a net emission of linear momentum that induces an acceleration on the merger remnant, which eventually can reach a recoil velocity up to several thousands of $km\,s^{-1}$. The final recoil velocity imparted to the remnant due to the relativistic kick is computed by ARWV with the following equation

$$\mathbf{v}_{recoil} = v_m \mathbf{e_1} + v_\perp (\cos\xi \mathbf{e_1} + \sin\xi \mathbf{e_2}) \tag{4.6}$$

where $\mathbf{e_1}$ is the unit vector pointing from the primary to the seconday binary component, while $\mathbf{e_2}$ is an orthogonal unit vector in the two-body orbital plane, such that the basis formed by $\mathbf{e_1}$, $\mathbf{e_2}$ and the orbital angular momentum is direct. The other terms are defined as

$$\begin{aligned} \xi =& a + bS_\parallel + c\delta_m \Delta_\parallel \\ v_m =& \eta^2 \delta_m (A + B\delta_m^2 + C\delta_m^4) \\ v_\perp =& H\eta^2 (\Delta_\parallel + H_{2a} S_\parallel \delta_m + H_{2b} \Delta_\parallel S_\parallel \\ &+ H_{3a} \Delta_\parallel^2 \delta_m + H_{3b} S_\parallel^2 \delta_m + H_{3c} \Delta_\parallel S_\parallel^2 \\ &+ H_{3d} \Delta_\parallel^3 + H_{3e} \Delta_\parallel \delta_m^2 + H_{4a} \Delta_\parallel^2 S_\parallel \delta_m \\ &+ H_{4b} S_\parallel^3 \delta_m + H_{4c} S_\parallel \delta_m^3 + H_{4d} \Delta_\parallel S_\parallel \delta_m^2 \\ &+ H_{4e} \Delta_\parallel S_\parallel^3 + H_{4f} \Delta_\parallel^3 S_\parallel) \end{aligned} \tag{4.7}$$

where a, b and c are dimensionless constants while A,B,C and H are constants given in $km\,s^{-1}$. The subscript $\parallel$ denotes the vector projections along the direction of the binary angular momentum vector. The constants are all reduced by numerical simulations carried in the original paper by Healy & Lousto (2018 [25]) that introduced this recoil prescription. For each BH in the simulation, ARWV accepts as input values the Cartasian projections of the BH dimensionless spin α_i with $|\alpha_i| \leq 1$. The recoil velocity depends

on the masses and the dimensionless spins of the progenitor BHs, which are implemented in equations 4.7 with the following factors

$$\begin{aligned} S &= \frac{\alpha_1 m_1^2 + \alpha_2 m_2^2}{m^2} = \frac{\alpha_2 + q^2 \alpha_1}{(1+q)^2} \\ \Delta &= \frac{\alpha_2 m_2 - \alpha_1 m_1}{m} = \frac{\alpha_2 - q\alpha_1}{1+q} \\ \eta &= \frac{m_1 m_2}{m^2} \\ \delta_m &= \frac{m_1 - m_2}{m} \leq 0 \end{aligned} \tag{4.8}$$

in which $m = m_1 + m_2$ is the total mass of the binary, $q = m_1/m_2 \leq 1$ is the mass ratio and $\alpha_{1,2}$ are the dimensionless spins of the BBH components.

4.2 Mock BBHs systems

We performed a total of 10^4 simulations, each of which recreates a three-body encounter between a BBH and a massive $\geq 60\,M_\odot$ black hole. The initial conditions have been generated exploiting a similar prescription to the one introduced by Hut & Bahcall (1983 [33]). Specifically, the binary is characterized by a primary and a secondary BH with masses m_1 and m_2, semi-major axis a and eccentricity e. The massive BH intruder has mass m_3, it approaches the binary starting from an infinity-distance D with an initial velocity relative to the center-of-mass of the binary v. The encounter strictly depends on the impact parameter b, the orbital phase of the binary f and the impact directions ϕ, θ and orientation ψ. The angle ϕ is defined as the angle between the pericenter of the binary orbit and the intersection of the vertical plane in which lies the initial velocity vector of the intruder. The angle θ defines the aperture included between the perpendicular versor of the binary orbital plane and the intruder initial velocity direction at infinity. The aperture ψ is instead the angle that defines the orientation of the impact parameter respect to the orbital plane direction in a surface perpendicular to the initial velocity of the intruder. Finally, each BH is characterized by a dimensionless spin $\alpha_i = |J_i|c/Gm_i^2$, where J is the BH spin, c is the speed of light, G is the universal gravitational constant, m_i is the mass of the BH and $i = 1, 2, 3$ is the index that refers respectively to the primary, secondary and intruder BH of the simulation. These initial parameters are schematically pictured in figure 4.1.

In principle, one could argue why we did not consider three-body encounters that include also stars. Since our main goal is to purely study dynamical interactions between black holes, we decided to focus only on encounters with already-formed BHs, avoiding in this way the stellar evolution

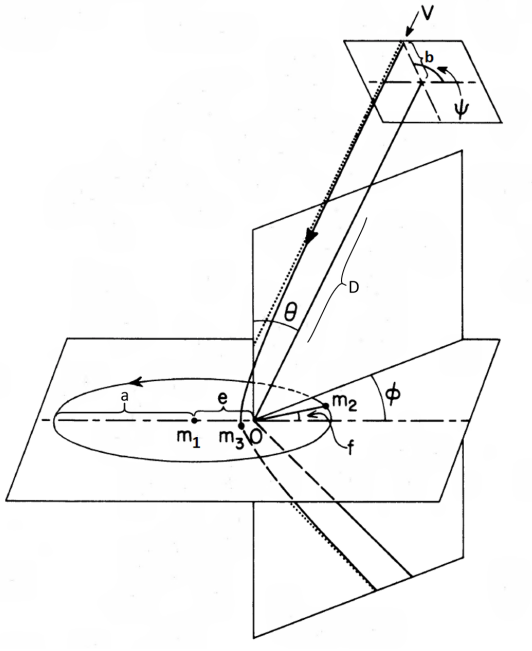

Figure 4.1: Initial parameters of the three-body encounters, from Hut & Bahcall 1983 [33].

part. The advantage of this choice is that we were able to run our simulations with ARWV without pairing it with a stellar evolution synthesis code. Stellar evolution complicates even more the problem, since it introduces other phenomena that can destroy the binary even before the BBH creation (e.g. supernova kicks). Therefore, in this preliminary study we decided to neglet stellar evolution to keep our analysis as simple as possible, but we will include it in the future development of this work.

Our simulations are set in young massive dense star clusters (YMCs) with a metallicity of $Z = 0.1\,Z_{\odot} \simeq 0.002$. In particular, we generated the initial conditions of the masses and semi-major axis from the data of the BHs population produced in the simulations of Di Carlo et al. (2019 [16]). They performed 10^4 simulations of YMCs at $Z = 0.002$ with masses in the range $10^3 \leq m_{cl}/M_{\odot} \leq 3 \times 10^4$ using the N-body code NBODY6++GPU coupled with the population synthesis code MOBSE. Their clusters, which evolved for a total time of $100\,Myr$, are characterized by an initial binary fraction of 0.4, a fractality prescription for the cluster's clumpiness and a Kroupa initial star mass function (Kroupa 2001 [40]) with minimum mass $0.1\,M_{\odot}$ and maximum mass $150\,M_{\odot}$. In their results they found 24 IMBHs, all of them formed from runaway collisions, in agreement with other studies

Parameter	Distribution	Range
m_1	KDE	$[3.2, 438.0]M_\odot$
m_2	KDE	$[3.0, 312.9]M_\odot$
m_3	KDE	$[3.0, 378.3]M_\odot$
a	Gaussian	$[0.059, 10^4]$AU
v	Maxwellian	...
e	e^2	[0, 1]
b	b^2	[0, 100]AU
D	Constant	...
ϕ	ϕ	$[0, 2\pi)$
θ	$\cos\theta$	[0, 1]
ψ	ψ	$[0, 2\pi)$
f	$\epsilon - e\cos\epsilon$	$[0, 2\pi)$
α_i	Maxwellian	...

Table 4.1: From left column to follow: the 13 initial parameters generated for each simulation, the distribution used to create the samples, the range of the distributions. For further details on each parameter see the next sections.

(e.g. Mapelli 2016 [51]). This confirms that runaway collisions and dynamics are both at work in YMSs, which are therefore a promising environment for the production of IMBHBs, as we argued in section 2.1.2.

Finally, we run each simulation for $10^5\,yr$. This amount of time is sufficiently long to ensure the energy exchange between the BBHs and the intruder while being also relatively short in computational time to allow the production of a statistical sample of simulations. The simulations have been run in parallel on 40 cores of DEMOBLACK, which is a cluster composed by 8 Intel Xeon Platinum 8168 at 2.70 GHz each of which with 24 cores, and a total of 14.7 TB of RAM memory plus 15.6 GB of Swap Memory.

In the next sections, we discuss the distributions and the methods that we used to sample each of the 13 initial parameters, which are resumed in table 4.1.

4.2.1 Masses m_1, m_2 and m_3

We extracted the masses of our black holes from the BH population produced in simulated YMSs after $100\,Myr$ by Di Carlo et al. (2019 [16]). The BHs produced by their simulations are formed via different channels along the

evolution of the cluster, therefore their masses span from few solar masses up to several hundreds. We first separated their mass values into single black holes and black holes bounded in binary systems, dividing these latter into primary and secondary cases. These three populations respectively range from $3.0\,M_\odot$ up to $378\,M_\odot$ for the 37049 single cases, and $3.0\,M_\odot$ up to $438\,M_\odot$ for the 2620 primaries, while the upper value is slightly lower $313\,M_\odot$ for the secondaries. Since we had to sample 10^4 values from each of these less-numerous groups, we exploited the kernel density estimation (KDE) method to compute the probability density function (PDF) for all the three populations. We then sampled the extracted PDF with the reject sampling technique to obtain the masses of all our synthetic BHs. In particular, the values for m_1 have been sampled from the PDF of the primaries, m_2 from the PDF of the secondaries and m_3 from the single BHs distribution extracted with the KDE. For m_3 we restricted the sampling to values with $m_3 \geq 60\,M_\odot$, otherwise our three-body encounters would have been dominated by low-mass $< 60\,M_\odot$ intruders. The resulting distribution of the masses sampled with this method are shown in figure 4.2.

4.2.2 Semi-Major Axis a

To use a self-consistent distribution for the semi-major axis of already formed BBHs, we made usage of the semi-major axis values of the BBHs produced by the simulations of Di Carlo et al. after $20\,Myr$ from the generation of their YMS clusters. In particular, we considered just SCs with masses in the range $8 \times 10^3 \leq m_{cl}/M_\odot \leq 3 \times 10^4$ since these have higher escapes velocities and can retain more BHs and BBHs that would be dynamically ejected. Furthermore, more massive clusters host a larger number of dynamical interactions and therefore, more hardening encounters that produce tight BBHs. The differences in the distribution of a between the full mass-range SCs of Di Carlo et al. and the restricted sample we used is shown in the upper plot of figure 4.3. We also checked that the distribution does not change significantly between 20 an 100 Myr. We thus performed a fit of the semi-major axis data with a gaussian distribution parameterized with mean value $\mu_a = 32.2\,AU$ and standard deviation $\sigma_a = 8.2\,AU$. We set the lower end of the distribution equal to the smaller semi-major axis of the data from Di Carlo et al., i.e. $a_{min} = 5.9 \times 10^{-2}\,AU$. As upper bound, we imposed instead the value $a_{max} = 10^4\,AU$ since larger values are typically of soft binaries that break very soon into an N-body simulation. Our final semi-major axis sample for the 10^4 simulations is shown in the bottom plot of figure 4.3.

A frequently used distribution in numerical simulations for the orbital periods and, therefore, for the semi-major axis, is the one extracted by Sana et al. (2012 [73]). They recovered a distribution $\mathcal{P}(T) \propto T^\alpha$ with $\alpha = -0.55$

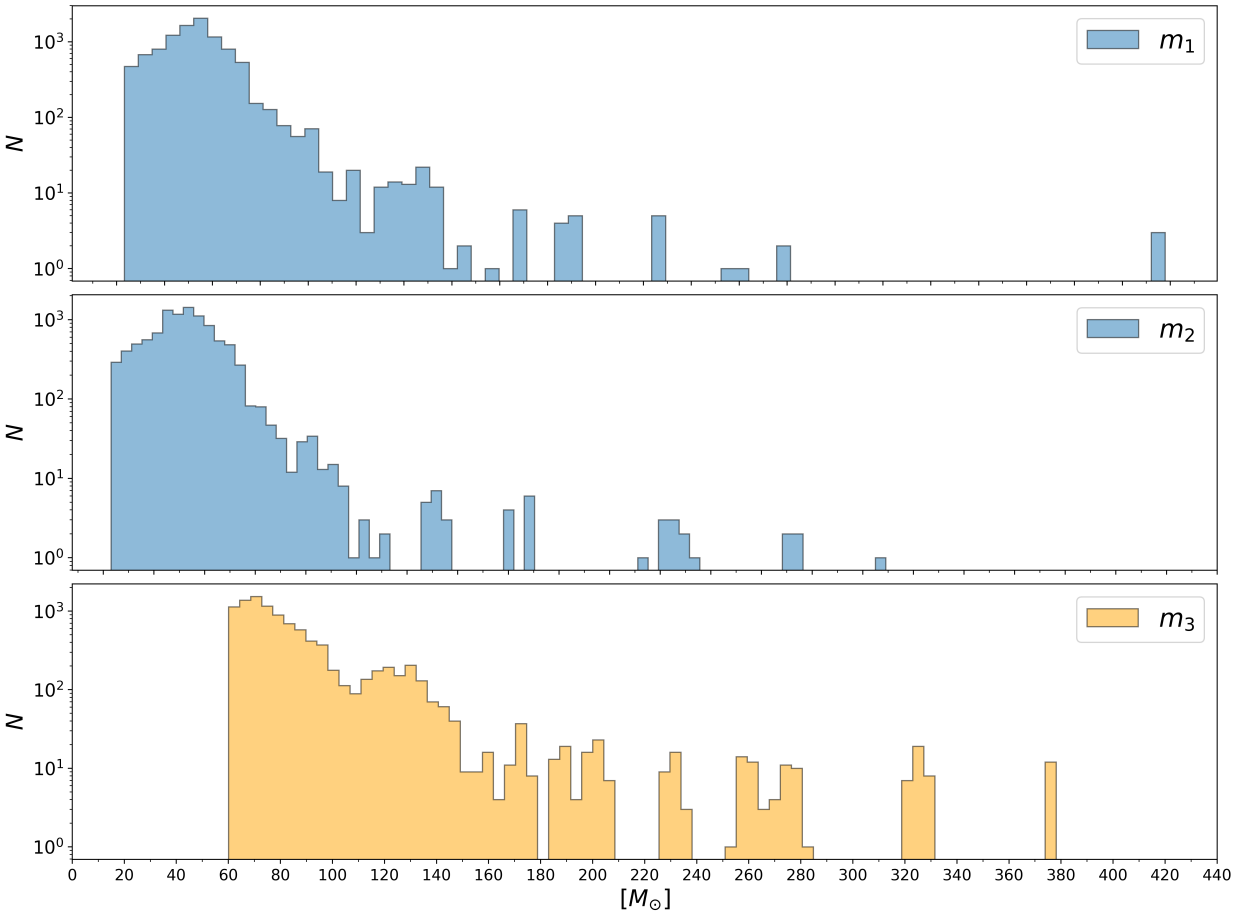

Figure 4.2: Mass distributions sampled from the BHs population of Di Carlo et al. (2019 [16]) using the kernel density estimation method. The upper plot refers to the primary component of the BBHs, the middle plot to the secondary and the bottom plot to the intruder. The last distribution is significantly shifted toward higher masses since we set a lower limit of $m_3 \geq 60\,M_\odot$.

from the observations of 40 nearby O type stars in spectroscopic binaries. We did not use this distribution since it is valid just for binaries of massive stars, while it is not a realistic choice for binaries of BHs. As comparison, we reported this distribution in the upper plot of figure 4.3.

4.2.3 Velocity v and Eccentricity e

The velocities of the BHs in a three-body encounter depend on the cluster dispersion velocity, and therefore on the cluster properties. In section 2.1.1 we have seen that the dynamical evolution of a star cluster is dominated by the two-body relaxation, which induces the cluster toward the thermalization. Since YMSs have a relaxation timescale $\leq 100\,Myr$ (see table 4.1), we can assume that the BHs in our simulations are in thermal equilibrium in the cluster and, therefore, that they follow the Maxwell-Boltzman distribution. We thus sampled the module of the relative initial velocity of the intruder from a thermal distribution with $\sigma = 5\,km\,s^{-1}$, which is a typical dispersion velocity value for such star clusters.

If stars are thermalized, binary eccentricities follow the thermal eccentricity distribution (Jeans 1919 [35], Ambartsumian 1937 [3], Heggie 1975 [28]), therefore we sampled the eccentricity values homogeneously on e^2 in the $[0, 1]$ range. The resulting samples are shown in the top right plot of figure 4.4.

4.2.4 Impact Parameter b and Initial Distance D

The impact parameter has been drawn according to an equal probability distribution $\propto b^2$ since it is proportional to the area of a surface element transverse to the direction of the intruder. The probability distribution has been taken between zero and the maximum value for which energy exchanges between the binary and the intruder are possible. This upper limit is thus extremely important for the outcome of the simulations since, too high values of b_{max}, would cause no or few interactions between the binary and the intruder. On the other hand, too small values would introduce a bias leading all the bodies to interact in each simulation. To estimate the most realistic upper bound of the distribution, we exploited the definition of b_{max} for a three-body encounter that we have introduced in section 2.2.2

$$b_{max} = \frac{\sqrt{2G(m_1 + m_2 + m_3)a}}{\sigma}. \tag{4.9}$$

For typical values such as $m_1 + m_2 + m_3 = 100\,M_\odot$, $a = 10\,AU$ and $\sigma = v = 10\,km\,s^{-1}$, we have that $b_{max} \simeq 100\,AU$. We thus set this value as upper end for the impact parameter distribution. The samples drawn from the distributions for all the simulations are shown in the bottom right plot

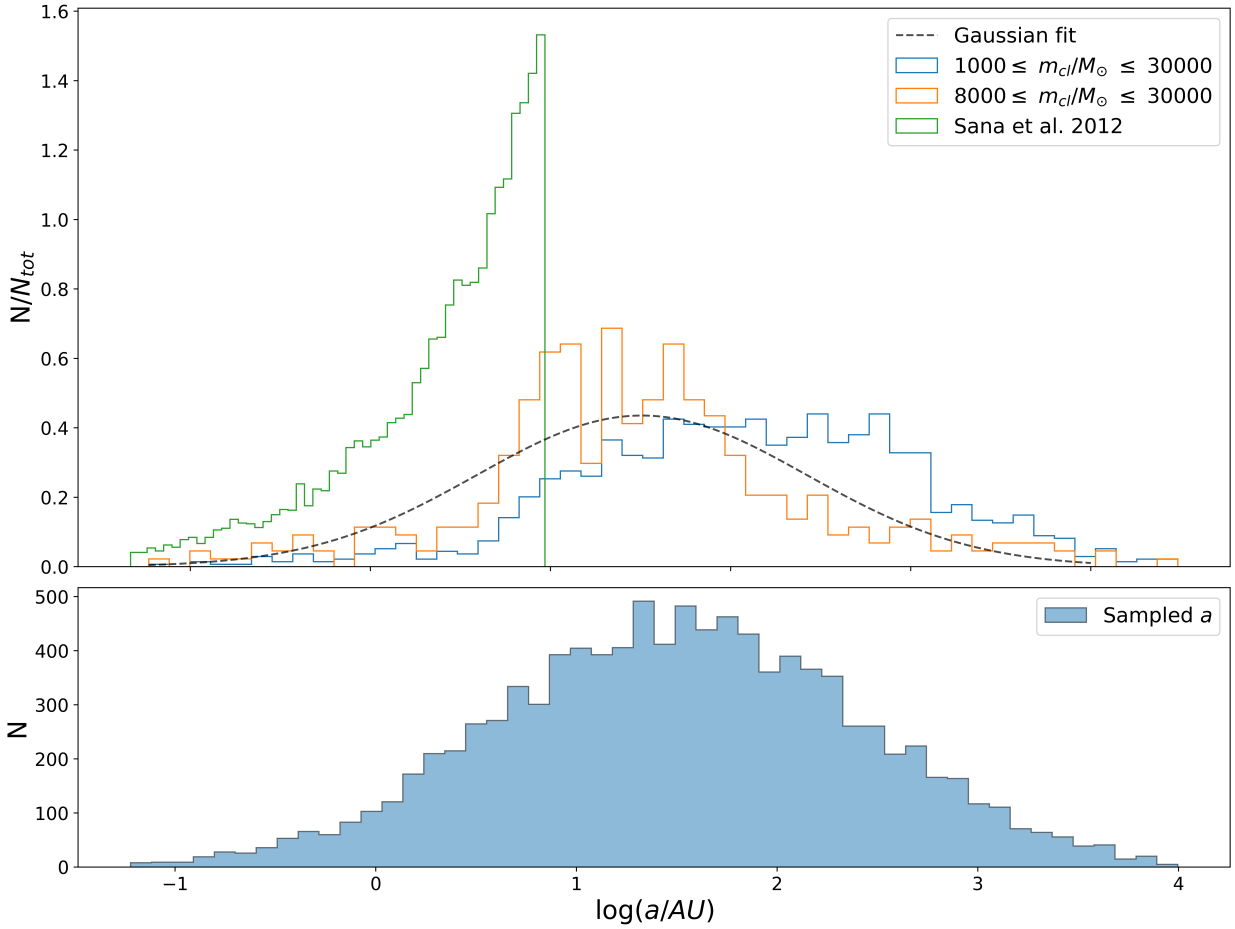

Figure 4.3: Upper plot: comparison between different semi-major axis samples. In blue, semi-major axis values of BBHs harbored in the simulated clusters of Di Carlo et al. (2019 [16]), where the mass of the clusters span from $10^3\,M_\odot$ up to $3 \times 10^4\,M_\odot$. In orange, a values from the simulations of Di Carlo et al. restricted only to massive YMSs with minimum mass $8 \times 10^3\,M_\odot$. Black dashed line, gaussian fit ($\mu_a = 32.3\,AU$, $\sigma_a = 8.2\,AU$) of the orange histogram. The orange distribution is shifted toward lower values of a respect to the blue one since more massive clusters have more dynamical encounters to harden the BBHs and higher escape velocities to retain them. Finally, in green we report also a population of binaries sampled from the distribution derived by Sana et al. (2012 [73]). This distribution favors low value of a respect to the gaussian choice. This follows from the fact that it has been reduced from the observation of binaries of stars that still have to experience events that lead to a growth of a (e.g. supernova explosions). Bottom plot: the distribution of the semi-major axis sampled from the gaussian fit for the 10^4 BBH in our simulations.

of figure 4.4.

Once set the impact parameter, we were able to introduce a prescription also for the initial distance of the intruder from the center of mass of the binary D (i.e. the spatial infinity of the simulations). The choice of this parameter has been carefully considered since the initial separation must be not too small and neither too high. The intruder must be set in fact at a spatial distance sufficiently high where the gravitational potential of the binary is negligible, to allow a "smooth" approach between the binary and the intruder in the simulations. On the other hand, D must be at a distance not too wide because realistically it could interact with another object of the cluster along the trajectory. For each simulation, we thus set D as the maximum value between $100 \cdot a$ and b. In this way, we fixed the irrealistic situation in which $b > D$ and at the same time we chose an initial distance that fulfills the considerations we have just discussed.

4.2.5 Direction ϕ, θ and orientation ψ Angles

The three angles have been generated according to the prescription adopted by Hut & Bahcall (1983 [33]). Specifically, we drafted the angles ϕ and ψ from homogeneous distributions in the interval $[0, 2\pi)$. For the direction angle θ, we instead sampled from a probability $\propto \cos\theta$ in the interval $[0, 1)$. All the angles sampled for the 10^4 simulations are shown in figure 4.5.

4.2.6 Orbital Phase f

The orbital phase f is defined as the angle with respect to the periastron which the secondary binary member would have at the time of the pericenter passage of the intruder. In other words, it is the projected true anomaly ϵ of the binary at the time that the intruder would have reached its hyperbolic pericenter. This definition can be expressed with the Keplerian mathematical expression

$$\frac{2\pi}{T} t_p = \epsilon - e \sin\epsilon \tag{4.10}$$

with T the period of the binary, e its eccentricity and t_p the time since the periastron passage. With this expression we random sampled ϵ and then extracted f with the following procedure. We first generated a random value in the range $[0, 2\pi)$ for the right term and we then exploited the bisection method to extract the zeros of the equation. Once reduced ϵ with the bisection, we then used it in the following expression to recover the orbital phase

$$\tan(f/2) = \left(\frac{1+e}{1-e}\right)^{1/2} \tan(\epsilon/2). \tag{4.11}$$

The final samples of the orbital phase drawn with this method for all the simulations are shown in the bottom right plot of figure 4.5.

4.2.7 Black Hole Spin α

We sampled the dimensionless spin magnitudes α for each BH in all the simulations following the prescription introduced by Bouffanais et al. (2019 [7]). The magnitude and direction of BH spins are still a matter of debate due to the large lack of knowledge for a relation between the BH spin magnitudes and the progenitor star spin. Furthermore, there are only poor spin constrains from the observations of aLIGO/aVirgo. Therefore, in general, two spin prescriptions are adopted: one which favors lower spin magnitudes, the "low-spin" prescription, and another which instead favors higher spin values, the "high-spin" prescription. Since the first two runs of aLigo/aVirgo disfavors distributions with large spin components aligned with the orbital angular momentum (The LIGO/Virgo Scientific Collaboration 2019 [86]), we adopted the low-spin model. In particular, we sampled α from a Maxwellian distribution with root mean square 0.1, and we then decomposed the dimensionless spin in its three Cartesian coordinates for each black hole. The drown spins used for the 3×10^4 simulated BHs are shown in the top left plot of figure 4.4.

4.2.8 Change of Coordinates

Once sampled all these initial conditions for the 10^4 simulations, it has been necessary to perform a change of coordinates and transform m_1, m_2, m_3, a, e, v, b, D, ϕ, θ, ψ and f in Cartesian coordinates rescaled in the reference frame of the three-body center-of-mass. The following expressions for the change of coordinates have been derived by Mapelli (2003 [47]), where the subscript $i = 1, 2, 3$ refers to the primary, secondary and intruder BHs.

$$
\begin{aligned}
x_1 &= -\frac{m_2}{(m_1+m_2)} \frac{a(1-e^2)\cos f}{(1+e\cos f)} \\
y_1 &= -\frac{m_2}{(m_1+m_2)} \frac{a(1-e^2)\sin f}{(1+e\cos f)} \\
z_1 &= 0
\end{aligned}
$$

$$
\begin{aligned}
\dot{x}_1 &= -\frac{m_2}{(m_1+m_2)} \left(\frac{e\cos f}{(1+e\cos f)} - 1 \right) \sin f \sqrt{\frac{G(m_1+m_2)}{a(1-e^2)}} (1+e\cos f) \\
\dot{y}_1 &= -\frac{m_2}{(m_1+m_2)} \left(\frac{e\sin^2 f}{(1+e\cos f)} + \cos f \right) \sqrt{\frac{G(m_1+m_2)}{a(1-e^2)}} (1+e\cos f) \\
\dot{z}_1 &= 0
\end{aligned}
$$

$$x_2 = \frac{m_2}{(m_1+m_2)}\frac{a(1-e^2)\cos f}{(1+e\cos f)}$$
$$y_2 = \frac{m_2}{(m_1+m_2)}\frac{a(1-e^2)\sin f}{(1+e\cos f)}$$
$$z_2 = 0$$

$$\dot{x}_2 = \frac{m_1}{(m_1+m_2)}\left(\frac{e\cos f}{(1+e\cos f)} - 1\right)\sin f\sqrt{\frac{G(m_1+m_2)}{a(1-e^2)}}(1+e\cos f)$$
$$\dot{y}_2 = \frac{m_1}{(m_1+m_2)}\left(\frac{e\sin^2 f}{(1+e\cos f)} + \cos f\right)\sqrt{\frac{G(m_1+m_2)}{a(1-e^2)}}(1+e\cos f)$$
$$\dot{z}_2 = 0$$

$$x_3 = D\left[\sin\phi\cos\psi\left(\frac{b}{D}\right) - \cos\phi\left(\sqrt{1-\left(\frac{b}{D}\right)^2}\sin\theta + \left(\frac{b}{D}\right)\cos\theta\sin\psi\right)\right]$$
$$y_3 = -D\left[\sin\phi\left(\sqrt{1-\left(\frac{b}{D}\right)^2}\sin\theta + \left(\frac{b}{D}\right)\cos\theta\sin\psi\right) + \left(\frac{b}{D}\right)\cos\phi\cos\psi\right]$$
$$z_3 = D\left(-\cos\theta\sqrt{1-\left(\frac{b}{D}\right)^2} + \left(\frac{b}{D}\right)\sin\theta\sin\psi\right)$$

$$\dot{x}_3 = v\sin\theta\cos\phi$$
$$\dot{y}_3 = v\sin\theta\sin\phi$$
$$\dot{z}_3 = v\cos\theta$$

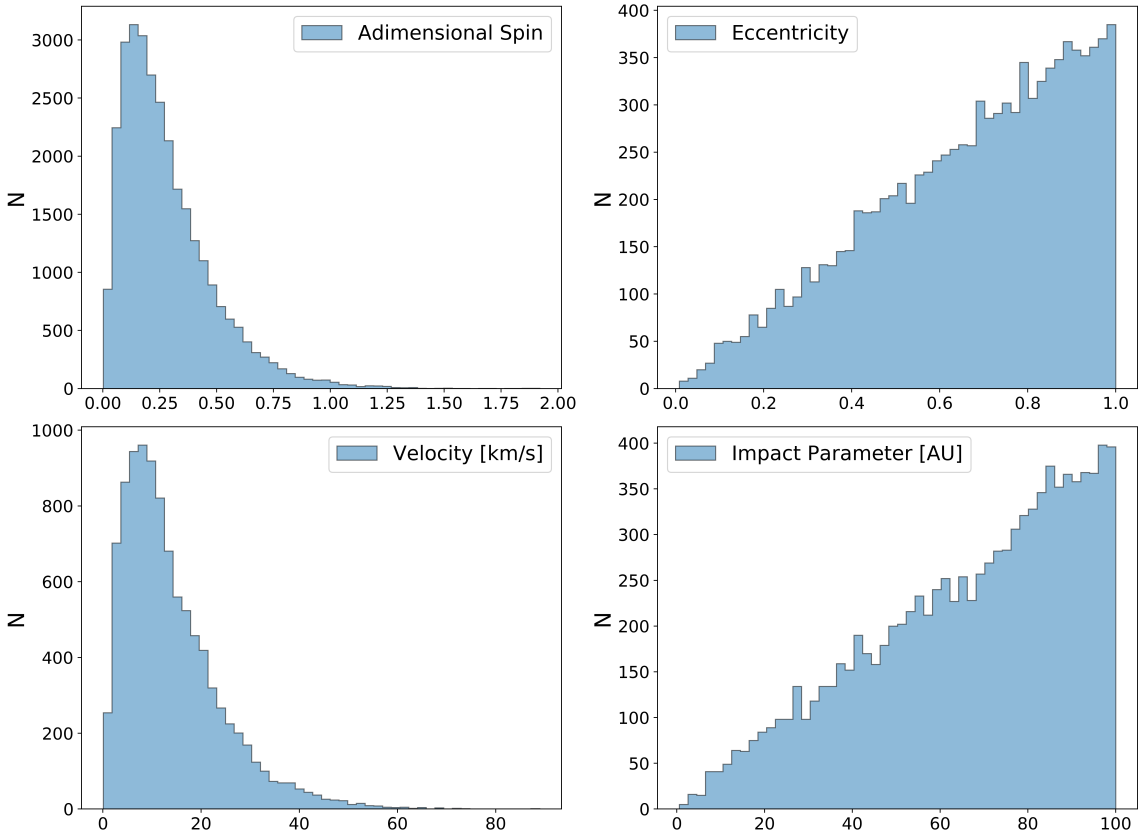

Figure 4.4: Values for some of the sampled initial parameters for the 10^4 simulatet three-body encounters. Top left: Adimensional spin α drawn from a Maxwell-Boltzman distribution with $\sigma = 0.1$. Top right: Eccentricity values sampled from a distribution $\propto e^2$ in the range [0,1]. Bottom left: initial magnitude velocity of the intruder v drawn from a Maxwell-Boltzman distribution with $\sigma = 5\,km\,s^{-1}$. Bottom right: Impact parameter b sampled from a distribution $\propto b^2$ in the range [0,100]AU.

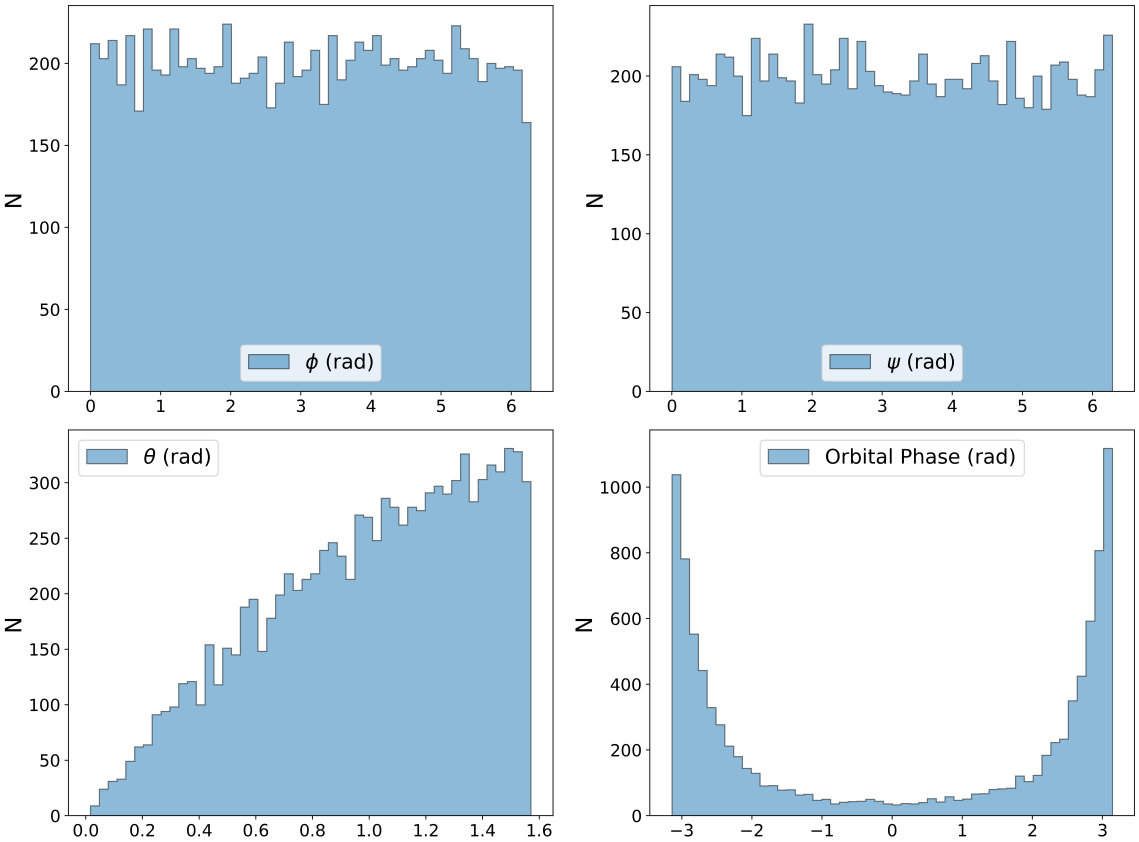

Figure 4.5: Same of figure 4.4. Top left and top right: values of the angles θ and ϕ homogeneously sampled in the [0,2π] range. Bottom left: θ angle drawn from a probability distribution $\propto \cos\theta$ in the range [0,1]. Bottom right: values for the orbital phase angle of the binary system in the range [$-\pi$,π] sampled with equation 4.11.

Chapter 5

Results

In this chapter, we present the results of the 10^4 three-body simulations performed with ARWV and generated with the initial conditions discussed in the previous chapter. In the first section we report the outcomes of the simulated dynamical encounters, while in the second section we focus on the properties of the BBHs resulting from the simulations.

5.1 Outcomes from three-body interactions

All the simulated three-body encounters between a BBH and a massive BH have been integrated by ARWV for 10^5 years. During this time, 55 pairs of BHs merge and consequently produce a massive BH remnant. Of these merger products, 8 have masses $> 100\,M_\odot$ and can be considered IMBHs while 25 of them lie above the lower end of the pair-instability mass gap in the range $60 \leq m_{BH}/\,M_\odot < 100$. The most massive BH produced by a merger in the simulations has $m_{BH} = 197\,M_\odot$, while the less massive one has $m_{BH} = 32\,M_\odot$.

In 18 cases, the merger remnant forms a new binary system with the third BH of the simulation to give birth to a second-generation BBH. Specifically, 17 second-generation BBHs are formed by the coalescence of the original binary[1] $m_1 - m_2$ and the massive intruder m_3, while in only 1 case the secondary BH m_2 of the original binary merges with m_3 and their product forms a new binary system with m_1. All of these 18 second-generation BBHs have at least one of the two members with $m_{BH} \geq 60\,M_\odot$, two of which have one IMBH component and can thus be considered IMBHBs, while in 1 case both the components of the second-generation BBH are IMBHs and the system can be classified as a binary IMBH. Among the other 37 mergers, no second generation BBHs are produced. In 34 of these simulations, the merger

[1] From now on, with original binary we will refer to the BBHs generated at the beginning of the simulations from the initial conditions. The primary and secondary components of these systems are called m_1 and m_2, while the massive intruder is m_3.

is reached by m_1 and m_2, while in the 3 remaining systems the merger is caused by the coalescence of m_1 and m_3.

Among the other 9945 simulations, we found that 1492 systems experience a fly-by encounter with the intruder BH. We define a fly-by encounter as a three-body interaction in which the three-body system configuration is the same before and after the dynamical encounter, or in other words, when m_1 and m_2 are still bound together at the end of the simulation while m_3 remains unbound. In 3979 cases, the original binary experiences an exchange where the secondary BH is kicked out from the system and a new $m_1 - m_3$ binary is born, while in other 3565 encounters the primary m_1 is replaced and the exchange produces a BBH with m_2 and m_3 as components. Lastly, we found 24 simulations in which all the BHs are bound together in a triple system and 145 cases where two of the three couples of BHs have a total energy $E < 0$ and the dynamical interaction is still going at 10^5 years. Specifically, 55 of these cases have $E_{13} < 0$ and $E_{23} < 0$, 14 systems have $E_{12} < 0$ and $E_{23} < 0$ while 76 have $E_{12} < 0$ and $E_{13} < 0$, with E_{ij} the total energy of the couple ij.

5.2 BBH Properties

At the end of the simulations, we obtained a total of 8984 BBHs, 55 of which merge during the simulation, while a further set of 381 BBHs merge after the end of the simulation but still within a Hubble time ($t_{coal} \leq t_H = 13.8 \times 10^9\, yr$). We are particularly interested in this population of merging BHs since it is the one that can be possibly detected with the gravitational waves observatories. We can discuss these merging BBHs in function of their outcomes from the simulations:

- Of the 55 mergers that happen during the simulations, 51 involve the coalescence between the primary and secondary BHs of the original binary. Of these, 11 had $t_{coal} \leq 10^5\, yr$ already before interacting with the intruder, and were already intended to merge during the simulation run. This means that all the other mergers between m_1 and m_2 have been triggered by the dynamical perturbations induced by the massive intruder m_3 on the original binary.

- Only 1 out of the 18 second-generation BBHs produced by the remnant of the merger and the third BH can reach coalescence within a Hubble time. This case provides a remarkable proof of the fact that the repeated merger scenario is indeed a valid formation path for massive black holes, and this is particularly important because we included relativistic kicks in our simulations.

- In 196 cases among the 1422 fly-bys, the original binary has $t_{coal} \leq t_H$ at the end of the dynamical interaction. 131 of these systems were

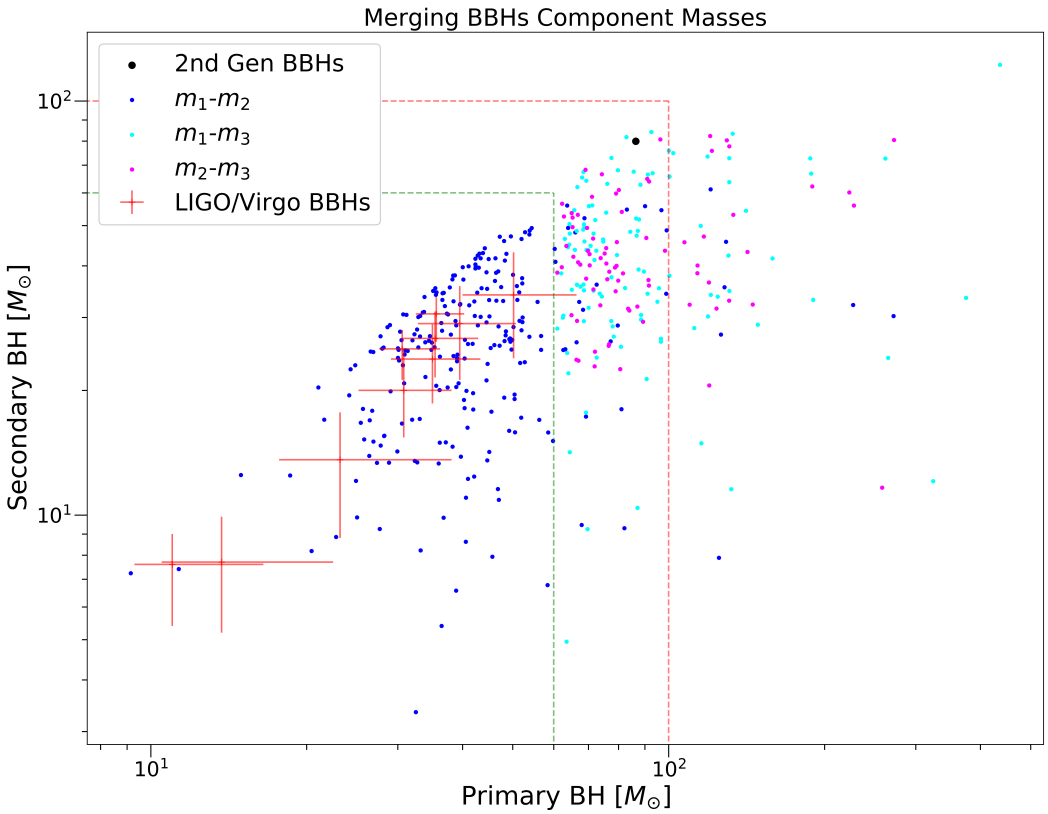

Figure 5.1: Primary (x-axis) vs secondary (y-axis) BH component masses of the 436 merging BBHs resulting from the simulations. Blue dots refer to the original merging BBHs, light blue dots represent merging BBHs composed of the primary of the original binary and the intruder, pink dots are the BBHs formed by the secondary BH of the original binary plus the intruder, while black dots are second-generation BBHs. The green and red dashed lines show the limits at $60\,M_\odot$ and $100\,M_\odot$. Binaries that lie in the region bounded between the red and green lines have at least one component in the pair-instability mass gap. BBHs outside the red-dashed limited region have at least one IMBH component and can be considered IMBHBs. Lastly, red crosses represent the 10 detections with relative errorbars of the mergers detected by aLIGO/aVirgo presented in the GWTC-1 catalog (The LIGO/Virgo Scientific Collaboration 2019 [84]).

already merging within a Hubble time even before the dynamical encounter with m_3, therefore at least 65 systems experienced a hardening process in which the semi-major axis of the original binary shrank as a consequence of the energy exchange with the intruder. This resulted in a reduction of the coalescence time for these systems.

- Among the 3979 cases in which the original binary experienced an exchange followed by the formation of a $m_1 - m_3$ BBH, 106 are newborn BBHs with a coalescence time smaller than the Hubble time.

- In the other 3565 exchanges in which the intruder replaced the primary, 78 binaries composed of m_2 and m_3 merge within a Hubble time.

All these 436 merging BBHs are reported in figure 5.1, which shows the masses of the BBH components. In the plot, we make no distinction between BBHs that merged during the simulations and BBHs with $t_{coal} \leq t_H$ after the three-body interaction. We, instead, classify our binaries based on the component masses at the end of the simulations. All the merging BBHs with both BHs less massive than $60\,M_\odot$ are original binaries that experienced a fly-by encounter. These systems are enclosed in the green-bounded region of the plot and are the result of a hardening interaction which caused the original binary to decrease its t_{coal} or even to merge. Only in few cases the merging BBHs $m_1 - m_2$ has the primary component above $60\,M_\odot$ or even $100\,M_\odot$. Interestingly, the only merging second-generation BBH in the simulations lies above the two green threshold boundaries since its components are both BHs in the pair-instability mass gap. This system is composed of a secondary BH with mass $80\,M_\odot$ generated from the merger of the original binary, and a primary BH with mass $86\,M_\odot$, which was the former intruder. Its components will eventually merge in $t_{coal} = 1.15 \times 10^5\,yr$ forming an IMBH. The evolution of this BBH is a perfect example of the repeated merger scenario and proves that sequential mergers can increase the mass of a BH, first up to the pair-instability gap, and then above $100\,M_\odot$, where it can be considered an IMBH.

In the plot we also reported the 10 merging BBHs detected by aLIGO/aVirgo with the corresponding error bars (Abbott et al. 2019 [84]), also reported in table 1.1 of chapter 1. All the observed binaries have BH components below the pair-instability gap limit, except for the primary of GW170729 which, with a mass of $50.2^{+16.2}_{-10.2}$ grazes the threshold with the errorbar.

Most of the binaries outside the green-dashed regions are BBHs that experienced an exchange, as expected since the intruders have all been generated with $m_3 \geq 60\,M_\odot$ as initial condition. In particular, the BBHs reported between the two colored-dashed lines in the plot are the 153 merging binaries out of the 6235 systems with at least one of the two components in the pair-instability mass gap found at the end of the simulations. For comparison, the binaries with at least one of the two BHs in the range

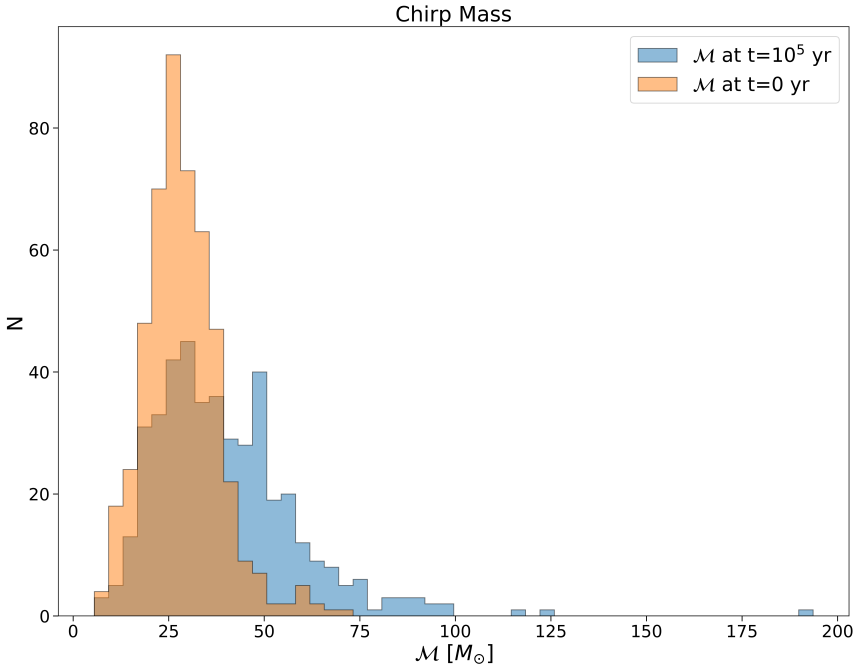

Figure 5.2: Orange histogram: Chirp masses of the 489 BBHs with $t_{coal} \leq t_H$ before the three-body interactions. Blue histogram: chirp masses of the 436 merging BBHs at the end of the simulations.

$60 \leq m_{BH}/M_\odot \leq 100$ were 665 before the dynamical encounter, only 38 of which were merging BBHs. All the BBHs lying beyond the red-dashed line have at least one IMBH component and can be considered IMBHBs. The plot shows all the 54 merging IMBHBs we recovered as a result of dynamical encounters, among the 1468 total IMBHBs produced by the three-body interactions. In contrast, the merging IMBHBs among the original binaries generated with the initial conditions were only 12 of the 155 BBHs with at least one IMBH. Finally, we found one case of merging BBH with two IMBHs as components (upper-right corner of the plot), where the primary mass has a value of $436\,M_\odot$, the secondary is $122\,M_\odot$ and the binary merges in $t_{coal} \simeq 1.43\,Myr$.

These last results lead to the conclusion that dynamics is one of the main drivers for the mass growth of the BBH components, and that it also contributes to increasing the number of merging BBHs with at least one of the two BH in the intermediate-mass range or the pair-instability mass gap. This is confirmed by figure 5.2, which reports the chirp mass $\mathcal{M} = (m_1 m_2)^{3/5}(m_1+m_1)^{-1/5}$ both for the 436 merging systems at the end of the simulations and for the 489 merging BBHs before the dynamical encounters. From this figure, it is apparent that dynamics enhances the chirp masses of

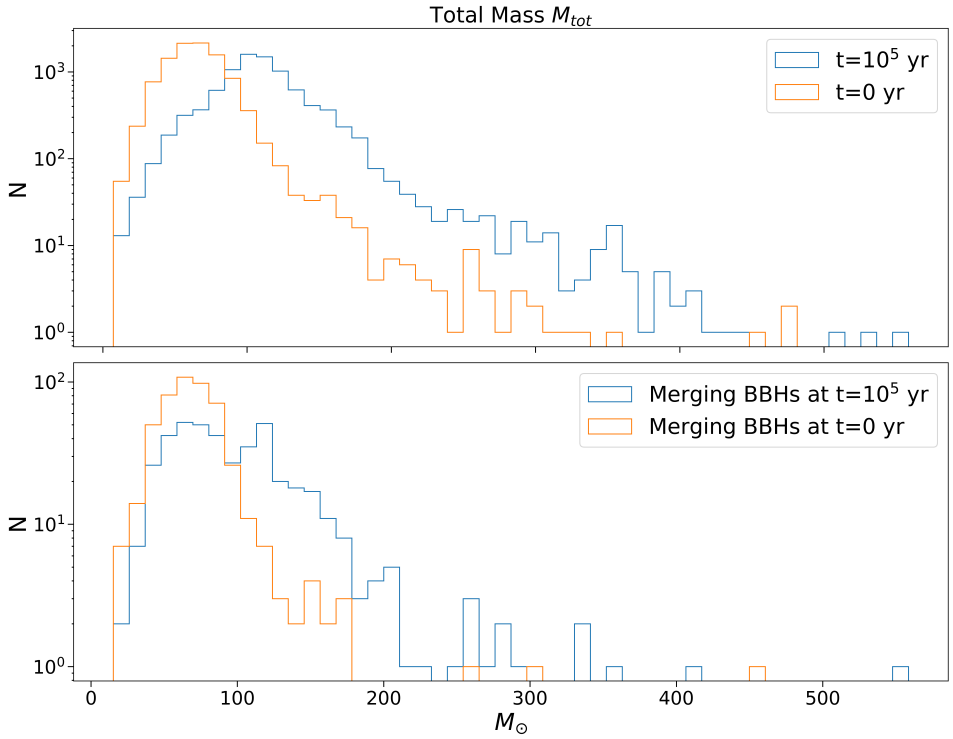

Figure 5.3: Upper panel: total mass of all the original binaries generated from the initial conditions at the beginning of the simulation (orange), vs total mass of the remaining BBHs at $10^5\,yr$ (blue), which include second-generation binaries and systems that experience fly-bys and exchanges. Bottom panel: same as the upper panel, but for binaries with $t_{coal} \leq t_H$ before (orange) and after (blue) the three-body encounter took place.

the merging systems up to a maximum value of $194\,M_\odot$, in contrast to the previous maximum value of $71\,M_\odot$.

Finally, the bottom panel of figure 5.3 shows the total mass M_{tot} of the merging binaries before and after the three-body encounters took place. Again, the dynamical interactions contribute to increasing the masses of these binaries mostly via exchange, where the massive BH intruder kicks out one of the two components to take its place. The overall effect is even more visible in the upper panel of the same figure, where we compared the total masses of all the 10^4 original binaries at the beginning of the simulations with the total masses of the remaining 8984 binaries after $10^5\,yr$ (these include second-generation BBHs and binaries that experienced fly-by and exchange encounters).

Besides the total mass, the three-body interactions favor the creation of binaries with unequal masses. This effect is evident in the upper panel of figure 5.4, which shows the mass ratio q of the original binaries in comparison

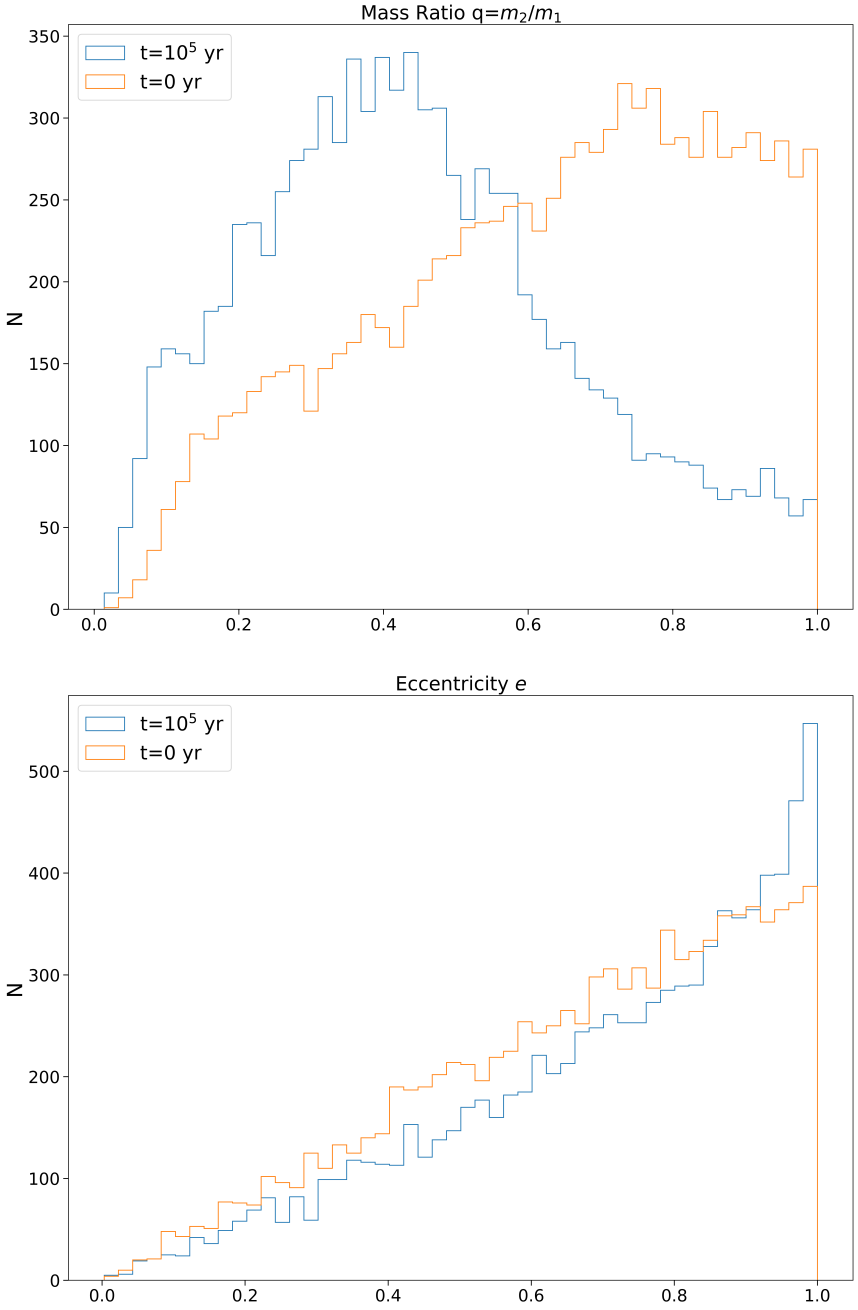

Figure 5.4: Upper panel: distributions of the BBHs mass ratio of the 10^4 binaries at the beginning of the simulation (orange) vs the 8984 remaining BBHs after the dynamical encounter (blue). Bottom panel: same as the upper panel but for the eccentricity values.

with the mass ratio of all the remaining binaries at the end of the simulations. All the exchange processes and the creation of second-generation BBHs have introduced more massive BHs in the binary components, which result in a decrease of the average mass ratio and in a change of the overall trend of the distribution toward lower values. Also the eccentricity distribution of the systems has changed. The bottom plot of figure 5.4 points out that BBHs formed as a consequence of dynamical interactions favor eccentricities close to 1. This trend comes from the fact that captured intruders in exchange processes can have high velocities respect to the original binary systems. Thus, the intruders can settle in eccentric orbits where they can replace one of the two components after several resonant encounters, and lead to the formation of an eccentric and more massive BBH. Lastly, figure 5.5 and figure 5.6 show the semi-major axis and the coalescence times for all the binaries at the beginning and the end of the simulations. The distribution of the semi-major axis presents only a small broadening effect, probably as a consequence of Heggie's law. This states that, statistically, tight binaries get tighter while wide binaries tend to become wider as a consequence of dynamical interactions (Heggie 1975 [28]). As to the coalescence time distributions, the difference between initial conditions and final distributions is more evident at shorter times. The original binaries include a tail of BBHs with $t_{coal} \lesssim 3 \times 10^4\, yr$ that is instead missing in the final BBHs distribution. Most of the binaries in the tail are among the 55 systems that merged during the 10^5 years of simulations, 37 of which produced a single black hole that does not contribute anymore to the distribution. In the other 18 cases in which the merger gave birth to a second-generation BBH, the new-born binary is still part of the blue histogram population but it has in general higher values of t_{coal}.

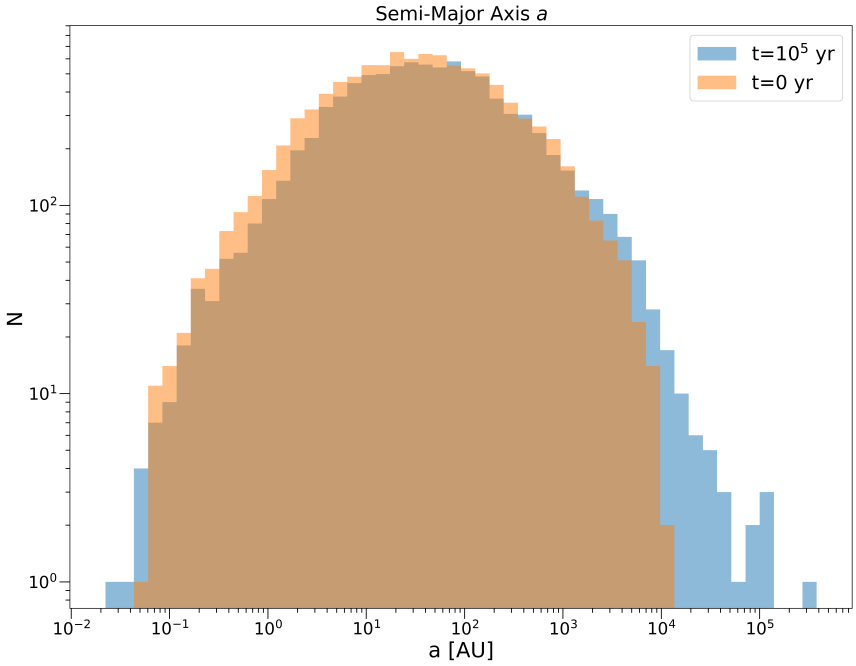

Figure 5.5: Distributions of the semi-major axis for the original binaries generated from the initial conditions (orange) and the population of BBHs formed during the simulations (blue).

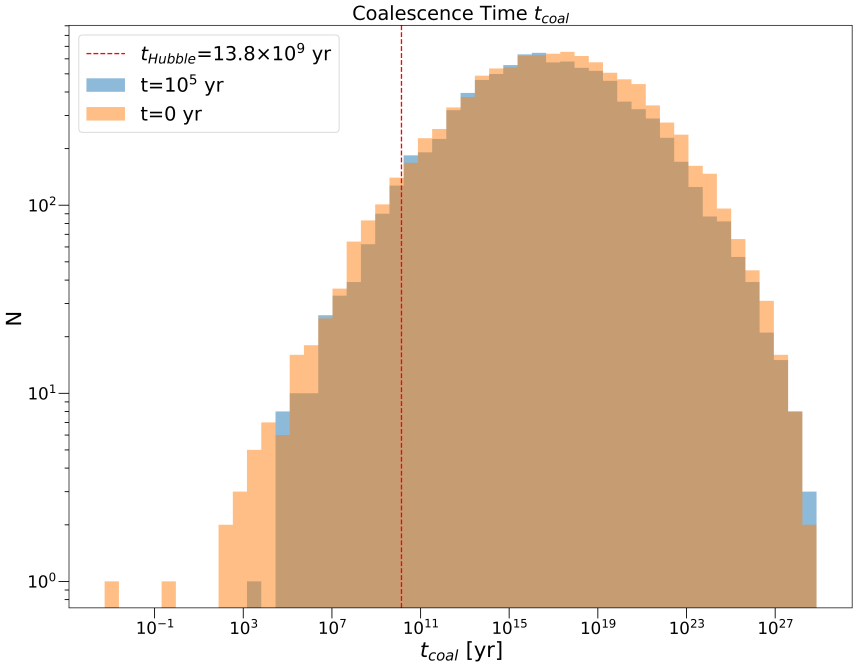

Figure 5.6: Same as figure 5.5 but for the coalescence times of the binaries. The vertical red-dashed line marks the limit below which a BBH merges within a Hubble time.

Chapter 6

Conclusions

Our knowledge in the field of black holes (BHs) has dramatically improved in the last few years thanks to gravitational-wave observations. However, the mass distribution of BHs still lacks data in the range $10^2 \leq m_{BH}/M_\odot \leq 10^5$. BHs lying in this mass range are classified as "intermediate-mass black holes" (IMBHs), which represent the connection between stellar-mass and supermassive black holes. In this work, we studied the demography of IMBHs, in particular, we focused on the dynamical interactions between black hole binaries (BBHs) and massive $\geq 60\,M_\odot$ BHs with the aim to explore the dynamical formation path of IMBHs and IMBH binaries (IMBHBs). With respect to previous work, we decided to study three-body encounters in young massive star clusters, which are good candidates as the IMBH birthplaces due to their high masses and active star formation, furthermore young massive star clusters are the most common birthplace of massive stars (Portegies Zwart et al. 2010 [68]).

We performed 10^4 simulations of three-body encounters with ARWV, a direct N-body code that implements a post-Newtonian approximation up to the 2.5 order to compute the equation of motion with extremely high precision even for close encounters. ARWV exploits the Mikkola's regularization algorithm for the integration, and includes a relativistic kick prescription for the post-merger BH remnant. We generated the initial conditions for the three-body encounters by exploiting self-consistent distributions, inferred from the simulations of young massive star clusters performed by Di Carlo et al. (2019 [16]).

During our simulations, 55 BBHs merged, 51 of which involved the coalescence of the original binary. Of these 51, 11 systems had $t_{coal} \leq 10^5\,yr$ before the three-body encounter took place; dynamics thus triggered the collision of the other 40 original systems. Furthermore, these mergers caused the formation of 8 remnants with $m_{BH} \geq 100\,M_\odot$ (which can be thus considered IMBHs) and 25 BHs above $60\,M_\odot$. In 18 cases, the merger product formed a binary system with the third BH, giving birth to a second-generation BBH.

In one case the newly-born BBH has $t_{coal} = 1.15 \times 10^5$ yr, less than a Hubble time, and has both components in the pair-instability mass gap. When these components merge, they give birth to an IMBH. This system is a remarkable result for two main reasons: firstly, it confirms that stellar-mass BHs can grow in mass via the repeated mergers scenario up to the formation of an IMBH. Secondly, it demonstrates that hierarchical growth of BHs to IMBHs can take place in young star clusters, even if the first coalescence event causes a strong relativistic kick on the BH remnant.

Besides this second-generation BBH, we found 380 binaries with $t_{coal} \leq t_H = 13.8\,Gyr$. Of these, 196 were hardened by the massive intruder (65 of them had coalescence timescale larger than the Hubble timescale before the encounter). The other 184 mergers are BBHs born from an exchange interaction, in which the intruder BH replaced one of the two components of the initial binary. These events affected the chirp mass distribution of the final mergers, which highly shifted toward larger values with respect to the initial distribution.

Dynamics has also increased the number of massive BBHs that merge within a Hubble time: the systems with at least one component in the range $60 \leq m_{BH}/M_\odot \leq 100$ passed from 38 before the three-body encounter up to 153 after the dynamical interaction, while the 12 initial IMBHBs increased to 54 at the end of the simulations. One of these systems is a binary with both members in the IMBH range and can be thus classified as binary IMBH. The existence of such merging systems will be probed by the next runs of LIGO and Virgo, by next-generation ground-based detectors (such as the Einstein Telescope or the Cosmic explorer), and by the space-born Laser Interferometer Space Antenna (LISA).

Finally, if we consider all (merging and non-merging) 8984 binary systems found at the end of the simulations, we find that dynamics has drastically increased the total mass and reduced the average mass ratio, while it favored the production of eccentric binaries.

From these results we can conclude that dynamics plays a key role in the production of massive binary systems, increasing the total mass and raising the number of massive BBH mergers. In the near future, we will continue the 169 simulations where the encounter was not concluded after $10^5\,yr$ (24 of which are triple systems), and we will include their outcomes in the existing sample of this work. As a future perspective, this study requires the implementation of stellar evolution in the simulations to better reproduce the physics of dynamical encounters in star clusters. This is indeed possible by coupling a population synthesis code to an $N-$body program, and only few studies have explored this path so far (e.g. Di Carlo et al. 2019 [16]). Lastly, it would be interesting to study dynamical encounters in even more dense environments, such as nuclear star clusters.

Appendices

Appendix A

IMBHs Electromagnetical Candidates

Here we present a list of the IMBH candidates in the mass range $10^2 \leq m_{BH}/M_\odot \lesssim 10^5$. For the origianal detections references see tables 2, 3 and 4 in Green et al. (2019 [24]).

IMBH Candidates Detected in Nuclei

Object	Dist [Mpc]	Method	m_{BH} $[M_\odot]$
NGC205	0.82	Dynamics	$(6.8^{+32}_{-2.2}) \times 10^3$
NGC5102	3.2	Dynamics	$(9.1^{+0.61}_{-0.51}) \times 10^5$
NGC5206	3.5	Dynamics	$(6.3^{+0.69}_{-0.61}) \times 10^5$
NGC4395	4.4	Dynamics	$(4.0^{+8}_{-3}) \times 10$
		RM	$(3.6 \pm 1.1) \times 10^5$
		RM	$(9.1^{+1.5}_{-1.6}) \times 10^3$
UGC 6728	27	RM	$(5.2 \pm 2.9) \times 10^5$
iPTF-16fnl	66.6	$m_{BH} - \sigma_{bulge}$	3.2×10^5
ASASSN-14ae	200	$m_{BH} - \sigma_{bulge}$	2.6×10^5
PTF-09axc	536	$m_{BH} - \sigma_{bulge}$	4.8×10^5
PS1-10jh	822	$m_{BH} - \sigma_{bulge}$	7.1×10^5
PTF-09djl	900	$m_{BH} - \sigma_{bulge}$	6.6×10^5
WINFS J1348	265	$m_{BH} - \sigma_{bulge}$	$5.1 - 5.6 \times 10^5$

Table A.1: Column from left to right: object name, distance in Mpc, method exploited for the measure and mass of the candidate IMBH. The reverberation mapping method is defined as RM. Empty rows refers to different mass measurements of the same object.

IMBH Candidates Outside Nuclei

Object	Dist [Mpc]	Method	m_{BH} $[M_\odot]$
47 Tuc	0.005	Dynamics	2300
		Dynamics	< 1650
		FP	< 1040
ω Cen	0.005	Dynamics	$(4.7 \pm 1.0) \times 10^4$
		Dynamics	$< 1.8 \times 10^4$
		Dynamics	< 1000
M64	0.007	Dynamics	(2000 ± 1000)
		FP	< 1130
NGC6624	0.008	Dynamics	> 7500
		Dynamics	< 650
		Dynamics	< 1000
		FP	< 1150
M15	0.010	Dynamics	1700-3200
		Dynamics	< 2000
		FP	< 1530
NGC6388	0.011	Dynamics	$(2.8 \pm 0.4) \times 10^4$
		Dynamics	< 2000
		FP	< 1770
NGC1904	0.013	Dynamics	(3000 ± 1000)
M54	0.024	Dynamics	9400
		Dynamics	1.1×10^4
		FP	< 3000
M31/G1	0.780	Dynamics	$(1.8 \pm 0.5) \times 10^4$
		FP	< 9700
HLX-1	95	X-ray	$10^4 - 2 \times 20^5$
		FP	$< 3 \times 10^6$
M82	3.5	X-ray	430 ± 100
		X-ray	< 100
NGC5252-ULX1	100	FP	$3000 - 2 \times 10^6$

Table A.2: Same of table A.1 but for candidates observed off-nuclei. The foundamental plane method is reported as FP.

Constraining Upper Limits

Object	Dist [Mpc]	Method	m_{BH} $[M_\odot]$
Fornax	0.135	Dynamics	$1 < \times 10^5$
UMi	0.076	Dynamics	$< 3 \times 10^4$
IC342	3.9	Dynamics	$< 3.3 \times 10^5$
NGC300	2.2	Dynamics	$< 1 \times 10^5$
NGC404	3.1	Dynamics	$< 1.5 \times 10^5$
NGC428	16.1	Dynamics	$< 7 \times 10^4$
NGC1493	11.4	Dynamics	$< 8.0 \times 10^5$
NGC2139	23.6	Dynamics	$< 4.0 \times 10^5$
NGC3423	14.6	Dynamics	$< 7.0 \times 10^5$
NGC4244	4.4	Dynamics	$< 5.0 \times 10^5$
NGC7424	10.9	Dynamics	$< 4.0 \times 10^5$
NGC7793	3.3	Dynamics	$< 8.0 \times 10^5$

Table A.3: Same of table A.1 but for candidates for which it has been reduced just an upper limit on the mass.

Appendix B

The Post-Newtonian Approximation

The Newtonian gravitational acceleration is a good approximation of the equation of motion for big distances, where BHs can be considered point-masses. However, our aim to analyze close encounters between black holes requires a more precise formalism of the equations of motion. In chapter 2 we have seen that dynamical encounters reduce the semi-major axis of the binaries via hardening interactions until gravitational waves emission becomes efficient. Newtonian dynamics does not have any prescription for this dissipative process, and we need therefore to include the general relativistic effects in the equations. The main problem is that deriving the equation of motion directly from Einstein's field equations is an overwhelming challenge due to their non-linear nature, and the problem complicates even more if we want to include the geometrical spacetime description of a complex system such as a three-body interaction between rotating BHs. The solution is to treat the effects of General Relativity as small perturbations of the leading Newtonian order, adding correction terms to the standard non-relativistic equations of motion. In our case, the prescription implemented by the code ARWV exploits the post-Newtonian (PN) formalism (Einstein, Infeld & Hoffmann 1938 [17]), which, on the assumption of weak gravitational field and motion of matter v slow compared to the speed of light c, consists in expanding the dynamics in powers of v/c. The PN expansion up to an order $(v/c)^{2n}$ is reported in the literature with the expression nPN, and it has proven to be remarkably effective in describing the dynamics of spiraling compact objects (Clifford 2011 [12]). ARWV implements a 2.5PN prescription (Mikkola & Merritt 2008 [60]), and exploits the formalism presented by Memmesheimer et al. (2004 [54]). In the paper, they present the reduced ordinary 3PN Hamiltonian of the system center-of-mass in the ADM coordinates (Arnowitt, Deser & Misner 1962 [5])

$$\mathcal{H}(\mathbf{r},\hat{\mathbf{p}}) = \mathcal{H}_0(\mathbf{r},\hat{\mathbf{p}}) + \frac{1}{c^2}\mathcal{H}_1(\mathbf{r},\hat{\mathbf{p}}) + \frac{1}{c^4}\mathcal{H}_2(\mathbf{r},\hat{\mathbf{p}}) + \frac{1}{c^6}\mathcal{H}_1(\mathbf{r},\hat{\mathbf{p}}). \tag{B.1}$$

The Newtonian ($\mathcal{H}_0$) and post-Newtonain ($\mathcal{H}_1$, $\mathcal{H}_2$ and $\mathcal{H}_3$) terms in equation B.1 are

$$\mathcal{H}_0(\mathbf{r},\hat{\mathbf{p}}) = \frac{\hat{\mathbf{p}}}{2} - \frac{1}{r} \tag{B.2}$$

$$\mathcal{H}_1(\mathbf{r},\hat{\mathbf{p}}) = \frac{1}{8}(3\eta-1)(\hat{\mathbf{p}}^2)^2 - \frac{1}{2}[(3+\eta)\hat{\mathbf{p}}^2 + \eta(\mathbf{n}\cdot\hat{\mathbf{p}})]\frac{1}{r} + \frac{1}{2r^2} \tag{B.3}$$

$$\begin{aligned}\mathcal{H}_2(\mathbf{r},\hat{\mathbf{p}}) =& \frac{1}{16}(1-5\eta+5\eta^2)(\hat{\mathbf{p}}^2)^3 + \frac{1}{8}\Big[(5-20\eta-3\eta^2)(\hat{\mathbf{p}}^2)^2 \\ &- 2\eta^2(\mathbf{n}\cdot\hat{\mathbf{p}})^2\hat{\mathbf{p}}^2 - 3\eta^2(\mathbf{n}\cdot\hat{\mathbf{p}})^4\Big]\frac{1}{r} + \frac{1}{2}\Big[(5+8\eta)\hat{\mathbf{p}}^2 \\ &+ 3\eta(\mathbf{n}\cdot\hat{\mathbf{p}})^2\Big]\frac{1}{r^2} - \frac{1}{4}(1+3\eta)\frac{1}{r^3}\end{aligned} \tag{B.4}$$

$$\begin{aligned}\mathcal{H}_3(\mathbf{r},\hat{\mathbf{p}}) =& \frac{1}{128}(-5+35\eta-70\eta^2+35\eta^3)(\hat{\mathbf{p}}^2)^4 \\ &+ \frac{1}{16}\Big[(-7+42\eta-53\eta^2-5\eta^2)(\hat{\mathbf{p}}^2)^3 \\ &+ (2-3\eta)\eta^2(\mathbf{n}\cdot\hat{\mathbf{p}})^2(\hat{\mathbf{p}}^2)^2 + 3(1-\eta)\eta^2(\mathbf{n}\cdot\hat{\mathbf{p}})^4\hat{\mathbf{p}}^2 \\ &- 5\eta^3(\mathbf{n}\cdot\hat{\mathbf{p}})^6\Big]\frac{1}{r} + \Big[\frac{1}{16}(-27+136\eta+109\eta^2)(\hat{\mathbf{p}}^2)^2 \\ &+ \frac{1}{16}(17+30\eta)\eta(\mathbf{n}\cdot\hat{\mathbf{p}})^2\hat{\mathbf{p}}^2 + \frac{1}{12}(5+43\eta)\eta(\mathbf{n}\cdot\hat{\mathbf{p}})^4\Big]\frac{1}{r^2} \\ &\Big\{\frac{1}{192}[-600+(3\pi^2-1340)\eta-552\eta^2]\hat{\mathbf{p}}^2 \\ &- \frac{1}{64}(340+3\pi^2+112\eta)\eta(\mathbf{n}\cdot\hat{\mathbf{p}})^2\Big\}\frac{1}{r^3} \\ &+ \frac{1}{96}[12+(872-63\pi^2)\eta]\frac{1}{r^4}\end{aligned} \tag{B.5}$$

In the above equations, $\mathbf{r} = \mathbf{R}/(GM)$, $r = |\mathbf{r}|$, $\mathbf{n} = \mathbf{r}/r$, $\hat{\mathbf{p}} = \mathbf{P}/\mu$, $M = m_1 + m_2$ is the total mass of the two bodies m_1 and m_2, $\mu = m_1 m_2/M$ is the reduced mass of the couple, $\eta = \mu/M$ is the finite mass ratio, $\mathbf{R}$ is the relative separation vector and $\mathbf{P}$ is its conjugate momentum vector. From each of these terms is then possible to reduce the equations of motion with

$$
\begin{aligned}
(\dot{r}_a^i)_n &= \frac{\partial}{\partial p_a^i}\mathcal{H}_n(\mathbf{r}_a, \hat{\mathbf{p}}_a) \\
(\dot{p}_a^i)_n &= -\frac{\partial}{\partial r_a^i}\mathcal{H}_n(\mathbf{p}_a, \hat{\mathbf{p}}_a)
\end{aligned}
\tag{B.6}
$$

where the subscript $a = 1, 2$ is for m_1 and m_2, n is the PN order and the superscript i is the component index.

Finally, the equations of motion can be rewritten as the expansion of the Newtonian acceleration with all the PN contributions $\mathbf{A}_{nPN}$ as

$$
\ddot{\mathbf{r}}_a = \frac{GM}{r^2}\left\{ -\mathbf{n} + \frac{1}{c^2}\mathbf{A}_{1PN} + \frac{1}{c^4}\mathbf{A}_{2PN} + \frac{1}{c^6}\mathbf{A}_{3PN} + \mathcal{O}\left(\frac{1}{c^7}\right)\right\}. \tag{B.7}
$$

Note that this formalism is a two-body formalism. Since we are running a three-body simulations, we have to apply it to each pair in the simulation (bodies 1 & 2, then bodies 1 & 3 and then bodies 2 & 3), separately.

Bibliography

[1] Abbott, B. P., Abbott, R., Abbott, T. D., et al. 2016, Physical Review Letters, 116, 241103

[2] Abbott et al., 2019, Phys. Rev. D 100, 064064

[3] Ambartsumian, V. A. 1937, Russian Astron. J., 14, 207

[4] Antonini, F., Chatterjee, S., Rodriguez, C., L., Morscher, M., Pattabiraman, B., Kalogera, V., & Rasio, F., A., 2016, ApJ, 816, 65

[5] Arnowitt, R., Deser, S., & Misner, C., W., 1962, arXiv:gr-qc/0405109

[6] Barnes, J., E., & Hut, P., 1986, Nature, 324, 466

[7] Bouffanais, Y., Mapelli, M., Gerosa, D., Di Carlo, U., N., Giacobbo, N., Berti, E., & Balbhav, V., 2019, ApJ, 886, n1

[8] Celoria, M, Olivieri, R., Sesana, A., & Mapelli, M., 2018, arXiv:1807.11489 [astro-ph.GA]

[9] Chandrasekhar, S. 1943, Astrophysical Journal, 97, 255

[10] Chassonnery , P., Capuzzo-Dolcetta, R., & Mikkola, S., 2019, `https://sites.google.com/uniroma1.it/astrogroup/hpc-html`

[11] Chatziioannou, K., et al., 2019, Phys. Rev., D 100, 104015

[12] Clifford, M., W., 2011, Proc. Nat. Acad. Sci., 108, 5938

[13] Crowther, P., A., et al., 2016, MNRAS 458, 624-659

[14] Chen, Y., Bressan, A., Girardi, L., et al. 2015, MNRAS, 452, 1068

[15] Colgate, S. A. 1967, Astrophysical Journal, 150, 163

[16] Di Carlo, U., N., Giacobbo, N., Mapelli, M., Pasquato, M., Spera, M., Wang, L., & Haardt, F., 2019, MNRAS, 487, 947–2960

[17] Einstein, A., Infeld, L., & Hoffmann, B., 1938, Ann. Math., 39, 65

[18] Freitag M., Guürkan M. A., Rasio F. A., 2006, MNRAS, 368, 141

[19] Fryer, C., L., 1999 Astrophysical Journal, 522, 413

[20] Fryer, C. L., Belczynski, K., Wiktorowicz, G., et al. 2012, Astrophysical Journal, 749, 91

[21] Gaburov, E., Lombardi, J. C., Jr., & Portegies Zwart, S. 2010, MNRAS, 402, 105

[22] Geha, M. et al. 1998, AJ, 115, 1045

[23] Giersz, M., Leigh, N., Hypki, A., Luützgendorf, N., & Askar, A. 2015, MNRAS, 454, 3150

[24] Greene, J., E., Strader, J., & Ho, L., C., 2019, Annual Reviews, arXiv:1911.09678

[25] Healy, J., & Lousto, C., O., 2018, Physical Re- view D, 97, 084002

[26] Heger, A, & Woosley, S. E., 2002, Astrophysical Journal, 567, 532-543

[27] Heger, A., Woosley, S. E., Fryer, C. L., & Langer, N. 2003, From Twilight to Highlight: The Physics of Supernovae, Springer, 3

[28] Heggie, D., C., 1975, MNRAS, 173, 729–787

[29] Hills, J., G., & Fullerton, L., W., 1980, Astrophysical Journal, 85, 1281–1291

[30] Hills, J., G., 1983, Astrophysical Journal, 88, 1269

[31] Holley-Bockelmann, K., Gültekin, K., Shoemaker, D., & Yunes, N. 2008, Astrophysical Journal, 686, 829-837

[32] Hurley, J. R., Tout, C. A., & Pols, O. R. 2002, MNRAS, 329, 897

[33] Hut, P., & Bahcall, J., N., 1983, ApJ, 268, 319–341

[34] Jani, K., Shoemaker, D., & Cutler, K., 2019, Nature Astronomy, 4, 260-265

[35] Jeans, J. H. 1919, MNRAS, 79, 408

[36] Kimball, C., Berry, C., P., L., & Kalogera, V., 2020, RNASS, 4(1):2

[37] Kimpson, T. O., Spera, M., Mapelli, M., & Ziosi, B. M. 2016, MNRAS, 463, 2443

[38] Kozai, Y. 1962, Astronomical Journal, 67, 591

[39] Koliopanos, F., 2018, Proceedingns of Science, arXiv:1801.01095

[40] Kroupa, P. 2001, MNRAS, 322, 231

[41] Kustaanheimo, P. & Stiefel, E., 1965, J. Reine Angew. Math., 218, 204

[42] Lada C. J., & Lada E. A., 2003, AR A&A, 41, 57

[43] Levi-Civita, T., 1920 ,Acta Mathematica, 42, 99

[44] Lidov, M. L. 1962, Planetary and Space Science, 9, 719

[45] Lousto, C. O., & Zlochower, Y. 2009, Physical Review Documents, 79, 064018

[46] Madau, P., & Rees, J., M., 2001, Astrophysical Journal, 551, L27

[47] Mapelli, M., 2003, Master Thesis, `http://web.pd.astro.it/mapelli/`

[48] Mapelli M., Ripamonti E., Zampieri L., Colpi M., Bressan A., 2010, MNRAS, 408, 234

[49] Mapelli, M., Ripamonti, E., Zampieri, L., & Colpi, M. 2011, MNRAS, 416, 1756

[50] Mapelli, M., Zampieri, L., Ripamonti, E., & Bressan, A. 2013, MNRAS, 429, 2298

[51] Mapelli, M. 2016, MNRAS, 459, 3432

[52] Mapelli, M. 2018, arXiv:1809.09130 [astro-ph.HE]

[53] Mapelli, M., & Giacobbo, N., 2018, MNRAS, 479, 4391

[54] Memmesheimer, R-M., Gopakumar A. & Schaäfer G., 2004, Physical Review D70:104011

[55] Mezcua, M., 2017, International Journal of Modern Physics D, 26, 11

[56] Mikkola, S., & Aarseth, S., J., 1990, Celestial Mechanics and Dynamical Astronomy, 47, 375

[57] Mikkola, S., & Aarseth, S., J., 1993, Celestial Mechanics and Dynamical Astronomy, 57, 439

[58] Mikkola, S., & Tanikawa, K., 1999, Celestial Mechanics and Dynamical Astronomy 74, 287-295

[59] Mikkola, S., & Aarseth, S., 2002, Celestial Mechanics and Dynamical Astronomy, 84, 343-354

[60] Mikkola, S., & Merritt, D., 2008, The Astronomical Journal 135, 2398-2405

[61] Miller, M. C., & Hamilton, D. P. 2002, MNRAS, 330, 232

[62] Nishizawa, A., Sesana, A., Berti, E. & Klein, A., 2017, MNRAS, 465, 4375-4380

[63] O'Connor, E., & Ott, C. D. 2011, Astrophysical Journal, 730, 70

[64] Peters, P. C. 1964, Physical Review, 136, 1224

[65] Portegies Zwart, S. F., Makino, J., McMillan, S. L. W., & Hut, P. 1999, A&A, 348, 117

[66] Portegies Zwart, S. F., & McMillan, S. L. W. 2002, Astrophysical Journal, 576, 899

[67] Portegies Zwart, S. F., Baumgardt, H., Hut, P., Makino, J., & McMillan, S. L. W. 2004, Nature, 428, 724

[68] Portegies Zwart, S. F., McMillan, S. L. W., & Gieles, M. 2010, Annual Review of A&A, 48, 431

[69] Quinlan G. D., 1996, New Astron., 1, 255

[70] Ramirez-Ruiz E., Rosswog S., 2009, Astrophysical Journal, 697, L77

[71] Rasskazov, A., Fragione, G. & Kocsis, B., 2019, arXiv:1912.07681

[72] Rodriguez, C., L., Chatterjee, S., & Rasio, F., A., 2016, PRD 93, 084029, 1602.02444.

[73] Sana H., et al., 2012, Science, 337, 444

[74] Sanders, R. H. 1970, Astrophysical Journal, 162, 791

[75] Sigurdsson S., Hernquist L., 1993, Nat, 364, 423

[76] Sigurdsson, S., & Phinney, E. S. 1993, ApJ, 415, S631

[77] Sigurdsson S., Phinney E. S., 1995, ApJS, 99, 609

[78] Spera, M., & Mapelli, M., 2017, MNRAS, 470, 4739

[79] Spera M., Mapelli M., Giacobbo N., Trani A. A., Bressan A., Costa G., 2018, preprint, (arXiv:1809.04605)

[80] Spitzer, L., Jr., & Hart, M. H., 1971, Astrophysical Journal, 164, 399

[81] Tang, J., Bressan, A., Rosenfield, P., et al. 2014, MNRAS, 445, 4287

[82] Tauris T. M., Langer N., Podsiadlowski P., 2015, MNRAS 451,2123

[83] The Event Horizon Telescope Collaboration, 2019, Astrophysical Journal, L1, 875

[84] The LIGO Scientific Collaboration & the Virgo Collaboration, 2019, Phys. Rev., X 9, 031040

[85] The LIGO Scientific Collaboration & the Virgo Collaboration, 2019, ApJ, 883, 2

[86] The LIGO Scientific Collaboration & the Virgo Collaboration, 2019, ApJ, 882, L24

[87] The LIGO Scientific Collaboration & the Virgo Collaboration, 2020, ApJL, arXiv:2001.01761

[88] The Planck Collaboration, 2018, arXiv:1807.06209 [astro-ph.CO]

[89] Vink, J. S., de Koter, A., & Lamers, H. J. G. L. M. 2001, Astronomy & Astrophysics, 369, 574

[90] Ziosi, B. M., Mapelli, M., Branchesi, M., & Tormen, G. 2014, MNRAS, 441, 3703

[91] Whalen, J., D., & Fryer, L., C., 2012, Astrophysical Journal, 756, L19

[92] Wise, J., H., 2012, ArXiv:1201.4820 [astro-ph.CO]

[93] Woosley S. E., 2017, ApJ, 836, 244

Acknowledgements

Un doveroso grazie a Michela Mapelli per essere stata una supervisor presente in ogni momento, ed avermi permesso di realizzare questo progetto integrandomi nel suo gruppo di ricerca e facendomi sentire parte del team.

Un enorme grazie ad Ugo, Yann, Sara ed Alessandro per avermi aiutato con consigli e suggerimenti, ed a tutti gli altri membri del gruppo DEMOBLACK: Filippo, Nicola, Stefano, Guglielmo, Mario e Giuliano.

Non basterebbero tutte le parole del mondo per ringraziare la persona che più ammiro tra tutte, ovvero Fra, che in questi 5 anni e mezzo di università si è spaccata in quattro per essere sempre lì al mio fianco a supportarmi in ogni occasione, nonostante la distanza.

Infine non posso che ringraziare i miei genitori, che mi hanno sempre sostenuto sotto ogni punto di vista senza mai mettere in discussione nessuna mia scelta di percorso, e per avermi reso la persona che sono. Vi devo molto. Dulcis in fundo ringrazio anche quel brigante di mio fratello Luca.

SEE YOU SPACE COWBOY ...